



**HAL**  
open science

## **Constraint on the time variation of the fine-structure constant with the SDSS-III/BOSS DR12 quasar sample**

Franco D. Albareti, Johan Comparat, Carlos M. Gutiérrez, Francisco Prada, Isabelle Pâris, David Schlegel, Martín López-Corredoira, Donald P. Schneider, Arturo Manchado, D. A. García-Hernández, et al.

### ► **To cite this version:**

Franco D. Albareti, Johan Comparat, Carlos M. Gutiérrez, Francisco Prada, Isabelle Pâris, et al.. Constraint on the time variation of the fine-structure constant with the SDSS-III/BOSS DR12 quasar sample. *Monthly Notices of the Royal Astronomical Society*, 2015, 452, pp.4153-4168. 10.1093/mnras/stv1406 . insu-03644715

**HAL Id: insu-03644715**

**<https://insu.hal.science/insu-03644715>**

Submitted on 25 Apr 2022

**HAL** is a multi-disciplinary open access archive for the deposit and dissemination of scientific research documents, whether they are published or not. The documents may come from teaching and research institutions in France or abroad, or from public or private research centers.

L'archive ouverte pluridisciplinaire **HAL**, est destinée au dépôt et à la diffusion de documents scientifiques de niveau recherche, publiés ou non, émanant des établissements d'enseignement et de recherche français ou étrangers, des laboratoires publics ou privés.

# Constraint on the time variation of the fine-structure constant with the SDSS-III/BOSS DR12 quasar sample

Franco D. Albareti,<sup>1</sup>★† Johan Comparat,<sup>1</sup> Carlos M. Gutiérrez,<sup>2,3</sup>  
 Francisco Prada,<sup>1,4,5</sup> Isabelle Pâris,<sup>6</sup> David Schlegel,<sup>7</sup> Martín López-Corredoira,<sup>2,3</sup>  
 Donald P. Schneider,<sup>8,9</sup> Arturo Manchado,<sup>2,3,10</sup> D. A. García-Hernández,<sup>2,3</sup>  
 Patrick Petitjean<sup>11</sup> and Jian Ge<sup>12</sup>

<sup>1</sup>*Instituto de Física Teórica (UAM/CSIC), Universidad Autónoma de Madrid, Cantoblanco, E-28049 Madrid, Spain*

<sup>2</sup>*Instituto de Astrofísica de Canarias (IAC), La Laguna, E-38205 Tenerife, Spain*

<sup>3</sup>*Departamento de Astrofísica, Universidad de La Laguna, La Laguna, E-38206 Tenerife, Spain*

<sup>4</sup>*Campus of International Excellence UAM+CSIC, Cantoblanco, E-28049 Madrid, Spain*

<sup>5</sup>*Instituto de Astrofísica de Andalucía (CSIC), Glorieta de la Astronomía, E-18080 Granada, Spain*

<sup>6</sup>*INAF, Osservatorio Astronomico di Trieste, Via G. B. Tiepolo 11, I-34131 Trieste, Italy*

<sup>7</sup>*Lawrence Berkeley National Laboratory, 1 Cyclotron Road, Berkeley, CA 94720, USA*

<sup>8</sup>*Department of Astronomy and Astrophysics, The Pennsylvania State University, University Park, PA 16802, USA*

<sup>9</sup>*Institute for Gravitation and the Cosmos, The Pennsylvania State University, University Park, PA 16802, USA*

<sup>10</sup>*CSIC, Spain*

<sup>11</sup>*Institut d'Astrophysique de Paris, CNRS-UPMC, UMR7095, 98bis bd Arago, F-75014 Paris, France*

<sup>12</sup>*Department of Astronomy, University of Florida, Gainesville, FL 32611-2055, USA*

Accepted 2015 June 23. Received 2015 June 23; in original form 2015 January 13

## ABSTRACT

From the Sloan Digital Sky Survey (SDSS) Data Release 12, which covers the full Baryonic Oscillation Spectroscopic Survey (BOSS) footprint, we investigate the possible variation of the fine-structure constant over cosmological time-scales. We analyse the largest quasar sample considered so far in the literature, which contains 13 175 spectra (10 363 from SDSS-III/BOSS DR12 + 2812 from SDSS-II DR7) with redshift  $z < 1$ . We apply the emission-line method on the [O III] doublet ( $\lambda\lambda$  4960, 5008 Å) and obtain  $\Delta\alpha/\alpha = (0.9 \pm 1.8) \times 10^{-5}$  for the relative variation of the fine-structure constant. We also investigate the possible sources of systematics: misidentification of the lines, sky OH lines, H  $\beta$  and broad line contamination, Gaussian and Voigt fitting profiles, optimal wavelength range for the Gaussian fits, chosen polynomial order for the continuum spectrum, signal-to-noise ratio and good quality of the fits. The uncertainty of the measurement is dominated by the sky subtraction. The results presented in this work, being systematics limited, have sufficient statistics to constrain robustly the variation of the fine-structure constant in redshift bins ( $\Delta z \approx 0.06$ ) over the last 7.9 Gyr. In addition, we study the [Ne III] doublet ( $\lambda\lambda$  3869, 3968 Å) present in 462 quasar spectra and discuss the systematic effects on using these emission lines to constrain the fine-structure constant variation. Better constraints on  $\Delta\alpha/\alpha$  ( $< 10^{-6}$ ) using the emission-line method would be possible with high-resolution spectroscopy and large galaxy/qso surveys.

**Key words:** line: profiles – surveys – quasars: emission lines – cosmology: observations – large-scale structure of Universe.

## 1 INTRODUCTION

Since Dirac's philosophical argument (Dirac 1937) against the fixed value of fundamental constants of Nature, several experiments have

been performed to constrain possible variations on dimensionless constants of physical theories. Fundamental constants of physics could be thought of as parameters which enter in our description of Nature but they cannot be predicted with our current theories and should be measured. Dirac's idea is based on the unlikely fact that the most fundamental constants of the Universe have a certain fixed value (at a given energy) with no apparent relation with the real world. It is more likely that their present values are the result of

\* 'la Caixa'-Severo Ochoa Scholar.

† E-mail: franco.albareti@uam.es

**Table 1.** Summary of the results obtained by recent works based on the [O III] emission-line method for the possible variation of the fine-structure constant.

| Reference                              | Quasar spectra | SDSS release                       | $z_{\min}$ | $z_{\max}$ | Time ago (Gyr) <sup>(a)</sup> | $\Delta\alpha/\alpha$ ( $\times 10^{-5}$ ) |
|--|----------------|------------------------------------|------------|------------|-------------------------------|--|
| Bahcall, Steinhardt & Schlegel (2004)  | 42             | EDR (Stoughton et al. 2002)        | 0.16       | 0.80       | 7.0                           | $7 \pm 14$                                 |
| Gutiérrez & López-Corredoira (2010)    | 1568           | DR6 (Adelman-McCarthy et al. 2008) | 0.00       | 0.80       | 7.0                           | $2.4 \pm 2.5$                              |
| Rahmani, Maheshwari & Srikanand (2014) | 2347           | DR7 (Abazajian et al. 2009)        | 0.02       | 0.74       | 6.7                           | $-2.1 \pm 1.6$                             |
| This work (2015)                       | 13 175         | DR12 (Alam et al. 2015)            | 0.04       | 1.00       | 7.9                           | $0.9 \pm 1.8$ <sup>(b)</sup>               |

Notes. <sup>(a)</sup> For a  $\Lambda$ CDM cosmology with  $H_0 = 67.8 \text{ km s}^{-1} \text{ Mpc}^{-1}$ ,  $\Omega_m = 0.31$  and  $\Omega_\Lambda = 0.69$  from *Planck*+*WMAP*-9+BAO (Planck Collaboration et al. 2014).

<sup>(b)</sup> Note: Since we have a larger sample than Gutiérrez & López-Corredoira (2010), we expect a factor  $\approx 2.5$  of improvement in the error just from purely statistical reasons. In Figs 9 and 10, it is shown that the error is dominated by the sky subtraction algorithm, which suggests that the performed analysis have reached the maximum precision with the available data.

a dynamical process, which had yielded the fundamental constants as they are measured today. Therefore, they should be considered as characterizing the state of the Universe (Uzan 2003). There are many current theoretical frameworks which allow for such variation of the fundamental constants, for instance, string theory (Maeda 1988), modified gravity and theories with extra dimensions (e.g. Clifton et al. 2012). Moreover, the experimental bounds on their variation have become a stringent test for those theoretical models (Thompson 2012; Leal, Martins & Ventura 2014). The most studied fundamental constants are the fine-structure constant  $\alpha$ , the Newton gravitational constant  $G$  and the electron-to-proton mass ratio  $\mu$  (Uzan 2003, 2011; García-Berro, Isern & Kubyshev 2007).

The fine-structure constant governs the electromagnetic coupling between photons and charged particles  $\alpha = e^2/(\hbar c)$ . The current constraint on its relative variation  $\Delta\alpha/\alpha$ , over geological time-scales, is  $|\Delta\alpha/\alpha| < 7 \times 10^{-8}$  up to  $z \approx 0.15$  (2 Gyr ago); obtained from the Oklo phenomenon (e.g. Petrov et al. 2006). It has also been reported  $|\Delta\alpha/\alpha| < 3 \times 10^{-7}$  up to  $z \approx 0.45$  (4–5 Gyr ago) from meteorites (Olive et al. 2002); which also excludes possible variations on the scales of the Solar system. On the other hand, there are also constraints,  $|\Delta\alpha/\alpha| \lesssim 10^{-2}$ , based on the cosmic microwave background (CMB; Landau & Scóccola 2010; Planck Collaboration et al. 2014) at  $z \approx 1100$  and from big bang nucleosynthesis, the latter being model-dependent. By measuring fine-structure multiplets at different redshift in the absorption or emission spectra of galaxies and quasars, located at different directions in the sky, one can measure an estimate of the variation of  $\alpha$  with time or space over cosmological scales.

The first measurements on the variation of  $\alpha$  from astronomical observations reached an accuracy of  $\Delta\alpha/\alpha \approx 10^{-2}$ – $10^{-3}$  (Svedoff 1956; Bahcall & Salpeter 1965; Bahcall & Schmidt 1967; Bahcall, Sargent & Schmidt 1967). Since then, the methodology and understanding of systematics has dramatically improved. Current measurements of absorption multiplets along the line of sight of three quasars around redshift 1.5, observed with spectral resolving power  $R \approx 60\,000$  at UVES/ESO-VLT, reached the  $\approx 5 \times 10^{-6}$  level (Evans et al. 2014). Using emission lines, an accuracy of  $\approx 2 \times 10^{-5}$  was achieved analysing 1500–2300 quasar spectra at  $z \approx 0.6$  (Gutiérrez & López-Corredoira 2010; Rahmani et al. 2014), taken with the Sloan Digital Sky Survey (SDSS)  $R \approx 2000$  spectrograph.

The measurements on absorption features on a quasar spectrum are currently limited by the precision in the absolute wavelength calibration of the spectra, i.e. 50–200 m s<sup>-1</sup> using spectra with  $R \approx 60\,000$  (Molaro et al. 2013; Evans et al. 2014; Whitmore & Murphy 2015). Furthermore, the so-called many-multiplet (MM) method used in Evans et al. (2014), although more precise, remains controversial as several assumptions are made, the most important one being ionization and chemical homogeneity. These assumptions may induce systematic biases on the value of  $\alpha$ .

In this article, we use the method based on the [O III] emission lines, first proposed by Bahcall & Salpeter (1965), which is less affected by systematics. In particular, there is no need for assuming ionization and chemical homogeneity, since the studied lines have the same profile (the transitions originate at the same upper energy level). Furthermore, the emission-line method suffers of much less spectral distortion, since the measurements of  $\Delta\alpha/\alpha$  are done on a spectral window  $\sim 100 \text{ \AA}$  as compared to  $\sim 1000 \text{ \AA}$  when the MM method is used. With a large ensemble of quasars and/or using high-resolution spectroscopy, the uncertainty can be reduced significantly, and will compete with the absorption method when using high-resolution spectroscopy.

The beginning of the SDSS survey opened a new era of precision, allowing us to use big samples of quasars; thus, reducing the statistical uncertainty of the measurement of  $\Delta\alpha/\alpha$  (see Table 1). Here, we extend these works by using the SDSS-III/BOSS Data Release 12 (SDSS-DR12; Alam et al. 2015), which covers the full Baryonic Oscillation Spectroscopic Survey (BOSS) survey footprint with an area coverage of 10 000 deg<sup>2</sup>. In contrast to these previous investigations, we use spectra obtained with the current BOSS spectrograph (Smee et al. 2013) instead of the previous SDSS-I/II instrument, making our BOSS sample totally independent from previous works. Moreover, the spectral range of the BOSS spectrograph allows an extension of the redshift interval for the [O III] doublet from  $z = 0.8$  to  $z = 1$ . The number of quasar spectra is increased by a factor of 5 with respect to SDSS-DR7. All these spectra have been visually inspected and classified as quasars by the BOSS collaboration, and their products are provided in the SDSS-III/BOSS Data Release 12 Quasar catalogue (DR12Q; see Páris et al., in preparation). For the final constraint on  $\Delta\alpha/\alpha$ , we combine in this work the BOSS sample with the previously studied SDSS-II DR7 quasar sample.

There are several emission doublets, in addition to [O III] ( $\lambda\lambda 4960, 5008 \text{ \AA}$ ), that can be used to measure  $\Delta\alpha/\alpha$  as noted by Bahcall et al. (2004), and first used by Grupe, Pradhan & Frank (2005). Gutiérrez & López-Corredoira (2010) analysed different doublets and found that the [Ne III] ( $\lambda\lambda 3869, 3968 \text{ \AA}$ ) and [Si II] ( $\lambda\lambda 6719, 6733 \text{ \AA}$ ) doublets appear in quasar spectra with sufficient frequency to have a meaningful sample. Results for [Si II] are consistent with no variation of the fine-structure constant, although the uncertainty is an order of magnitude bigger than for [O III], and this doublet can only be used at low redshift  $< 0.4$  for optical spectra. However, they obtained a positive variation of the fine-structure constant,  $\Delta\alpha/\alpha = (34 \pm 1) \times 10^{-4}$ , when the [Ne III] lines are used. No explanation was found for this positive variation. In this work, we also analyse the [Ne III] lines to check whether the same effect is present in our BOSS quasar sample.

There are investigations which use Si IV absorption lines ( $\lambda\lambda 1394, 1403 \text{ \AA}$ ) to obtain a precision of  $4 \times 10^{-6}$  (Chand et al. 2005). This method also avoids the assumption of ionization and

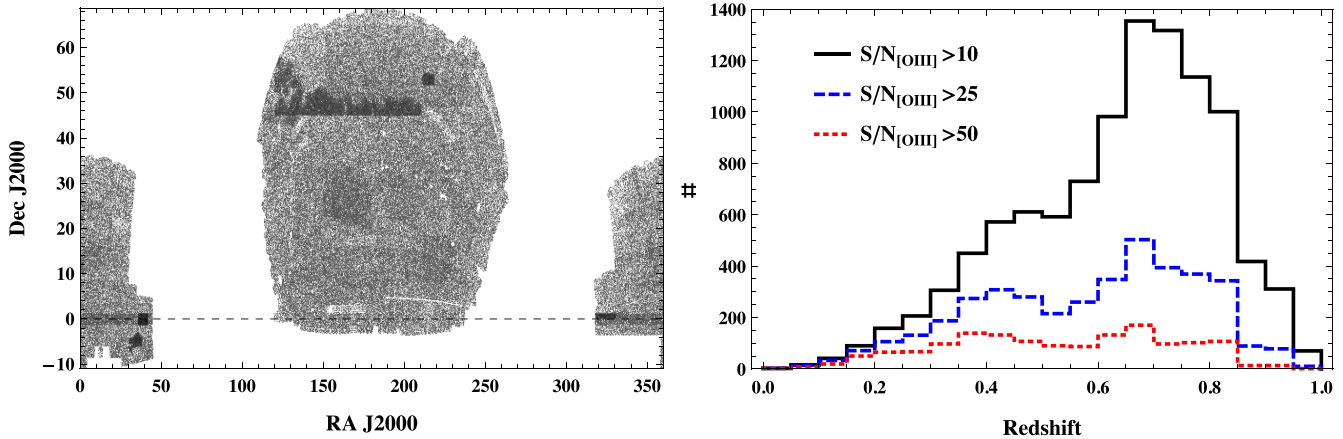


**Figure 1.** Left-hand panel: sky distribution of the full SDSS-III/BOSS DR12Q quasars (297 301) in J2000 equatorial coordinates. Right-hand panel: number of quasars with [O III] emission lines in our fiducial sample (10 363 quasars) in  $\Delta z = 0.05$  bins.  $S/N_{[\text{O III}]}_{5008} > 10$  (10 363 quasars), black solid line;  $S/N_{[\text{O III}]}_{5008} > 25$  (4015 quasars), blue dashed line; and  $S/N_{[\text{O III}]}_{5008} > 50$  (1498 quasars), red dotted line.

chemical homogeneity. However, since the separation between both lines is only  $\approx 9 \text{ \AA}$ , the wavelength precision needed in the laboratory for the separation between both lines is five times higher than using [O III] lines. Nevertheless, these constraints apply to the redshift interval  $1.59 < z < 2.92$ , which does not overlap with our range, thus they are complementary to the ones reported in this research.

Finally, in the light of the upcoming large galaxy surveys, like eBOSS and DESI, that will provide millions of high-redshift galaxy spectra, we also discuss using galaxies instead of quasars to set constraints on the fine-structure constant.

The paper is organized as follows. First, in Section 2, we describe the data set used for our analysis. Next, in Section 3, the methodology is presented, the emission-line method is explained, and the code and simulations to analyse the spectra are described. In Section 4, we study several samples to check for systematics. Then, our results are presented in Section 5. Finally, we provide in Section 6 a summary of the main conclusions achieved with this research project.

## 2 SAMPLE DESCRIPTION

All the spectra used in this investigation were downloaded from the SDSS Database. This survey (York et al. 2000), which began taking observations in 1998, consists of a massive collection of optical images and spectra from astronomical objects including stars, galaxies and quasars. For this purpose, there is a dedicated 2.5-m wide-angle optical telescope at Apache Point Observatory in New Mexico (USA; for more details, see Gunn et al. 2006). The third phase of this project (SDSS-III; Eisenstein et al. 2011) includes BOSS (Dawson et al. 2013) among its four main surveys. The data analysed in this research were provided by BOSS, and it is used for measuring  $\Delta\alpha/\alpha$  for the first time. The SDSS-III/BOSS pipeline (Bolton et al. 2012) classifies the objects as quasars with a  $\chi^2$  minimization procedure to fit the observed spectrum to multiple galaxy and quasar spectrum templates for all allowed redshifts. Then, a visually-inspected quasar catalogue is built from these objects. Our fiducial sample is obtained from the DR12Q catalogue version (Pâris et al., in preparation).

The wavelength coverage of the SDSS-III/BOSS spectrograph is 3600–10 400  $\text{\AA}$  and that of the SDSS-II spectrograph is

3800–9200  $\text{\AA}$ . The BOSS sample is homogeneous since all the spectra have been obtained with the same instrument, and it is independent from previous investigations. The wider coverage of the new spectra allows consideration of higher redshifts (up to  $z = 1$  for [O III] doublet) than in the previous SDSS-II analysis based on the same method (see Table 1). The BOSS spectrograph has two channels (blue and red) whose wavelength coverage is 3600–6350  $\text{\AA}$  and 5650–10 400  $\text{\AA}$ , respectively. The resolving power ranges from 1560 at 3700  $\text{\AA}$  to 2270 at 6000  $\text{\AA}$  (blue channel) and from 1850 at 6000  $\text{\AA}$  to 2650 at 9000  $\text{\AA}$  (red channel). For our sample, the [O III] lines fall in the red channel for >96 per cent of the quasars. The number of pixels of each spectrum is about 4600 for the BOSS spectra and 3800 for the SDSS-I/II spectra. The pixel spacing is uniform in log-wavelengths ( $\Delta \log \lambda = 10^{-4}$  dex). More complete information about the SDSS-I/II and BOSS spectrographs can be found in Smee et al. (2013).

### 2.1 Data selection

The SDSS-III/BOSS DR12Q catalogue contains 297 301 objects. Fig. 1 (left-hand panel) shows the quasar distribution in the sky. We summarize below the main selection criteria in order to define our fiducial sample from this catalogue.

(i) Redshift  $< 1$ . This limitation is imposed by the wavelength range of the BOSS optical spectrograph and the position of the [O III] lines. This criterion decreases the sample down to 45 802 quasars.

(ii)  $S/N_{[\text{O III}]}_{5008} > 10$ . We impose a mild constraint on the signal-to-noise ratio (S/N) of the stronger [O III] line (5008  $\text{\AA}$ ) in order to preserve a large number of spectra. Constraints on the expected width and amplitudes of the lines help in avoiding misidentifications of the [O III] doublet (see Section 4). This selection reduces the sample from 45 802 to 13 023 objects.

(iii) Non-converging fits. Since we analyse spectra with low S/N, there are some cases where the Gaussian fit to the lines does not converge. 1244 spectra are discarded, leaving us with 11 779 spectra.

(iv) Sky emission lines. Strong atmospheric lines, for instance the O I 5578  $\text{\AA}$  line, are poorly or not completely removed by the SDSS sky subtraction algorithm. This may lead to a wrong identification of the [O III] lines and to include low  $S/N_{[\text{O III}]}$  spectra (Gutiérrez

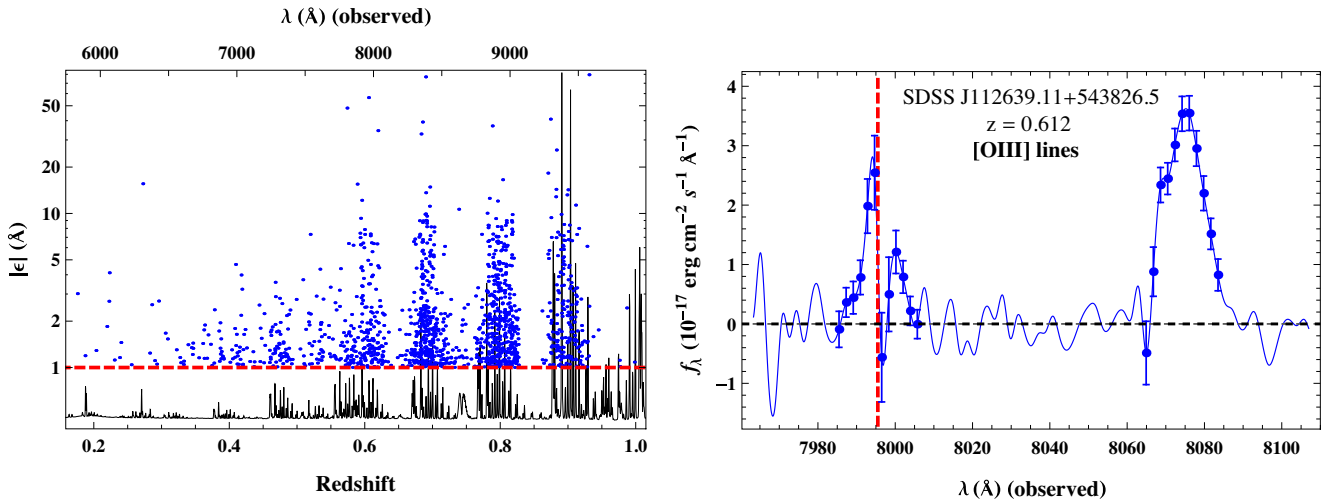


**Figure 2.** Left-hand panel: data points (1416) for which  $|\epsilon| = |\delta\lambda_z/(1+z) - \delta\lambda_0|$ , namely the absolute value of the difference between the measured line separation at redshift  $z$  in rest frame and the local one, is bigger than  $1 \text{ \AA}$  plotted as a function of redshift (and the wavelength observed for [O III] 4960). We compare with a typical sky spectrum: the [O III] positions for these spectra correlate with the sky emission lines. Hence, these high values of  $|\epsilon|$  are due to bad sky subtractions and/or low S/N. These spectra are removed. Right-hand panel: a spectrum removed from the sample because of the sky emission-line criteria. For this quasar, we get  $\epsilon = 1.2 \pm 0.6 \text{ \AA}$ . The weak [O III] line is affected by the subtraction of the  $7995 \text{ \AA}$  OH sky emission line, indicated by the vertical red dashed line.

& López-Corredoira 2010). Both effects will produce outliers. We use the SDSS sky mask for Ly $\alpha$  forest studies which contains 872 lines (see Delubac et al. 2015 for more details) to remove spectra whose [O III] lines lie within a particular distance from the strongest sky lines. Even though we vary the distance [O III] – sky lines, use different set of sky lines (according to their intensity), or evaluate other conditions (S/N, fit errors, etc.) to remove affected spectra; we usually eliminate 3–5 good spectra for each bad spectra eliminated. Thus, these tests decrease significantly the number of quasars while not being very effective: typically 50 per cent of the outliers are not removed. Thus, we decided to eliminate all spectra for which the separation between both lines differ by more than  $1 \text{ \AA}$  from the local value (see the last paragraph in Section 3.3). Fig. 2 (left-hand panel) shows that the distribution of these outliers is correlated with a typical sky spectrum. From a visual inspection, we observed that these spectra have low S/N, and they are in fact contaminated by sky emission line subtraction (see right-hand panel of Fig. 2). This effect causes us to discard 1416 spectra (12 per cent of the previous 11 779 quasars). Finally, we have 10 363 quasar spectra (our ‘fiducial sample’).

The presence of broad H  $\beta$  emission line ( $4861 \text{ \AA}$ ) near the weak [O III] line  $4960 \text{ \AA}$  could produce a blueshift in the determination of the [O III] line position. This could mimic a positive variation on the fine-structure constant. Therefore, a constraint on the strength and/or width of the H  $\beta$  emission line has been imposed on previous investigations (Bahcall et al. 2004; Gutiérrez & López-Corredoira 2010; Rahmani et al. 2014). However, we do not restrict any characteristic of the H  $\beta$  line in our fiducial sample. We obtain a weighted mean for  $\Delta\alpha/\alpha$  using as weights the uncertainty in  $\Delta\alpha/\alpha$  computed with the standard errors for the position of the lines derived from the Gaussian fits. The contamination of H  $\beta$  is automatically taken into account. For instance, a broad H  $\beta$  line near the [O III]  $4960 \text{ \AA}$  line means a bad Gaussian fit. Thus, we obtain larger errors in the position of the line centroids and, consequently, in  $\Delta\alpha/\alpha$ . In Section 4, we analyse several samples where the  $S/N_{H\beta}$  is constrained

to check that the H  $\beta$  contamination has little weight on the final constraint value.

An electronic table is published along with the paper which contains all the information of each spectrum from our fiducial sample of 10 363 quasars (see Appendix A).

The distribution of the selected quasars in redshift according to their selected  $S/N_{[O\text{III}]_{5008}}$  is plotted in Fig. 1 (right-hand panel). Fig. 3 (left-hand panel) displays a composite image built with all the spectra from our fiducial sample sorted by redshift. The right-hand panel shows the [O III] doublet in rest frame.

### 3 METHODOLOGY

#### 3.1 Measurement method

To first order, the difference between the energy levels of an atom is proportional to  $\alpha^2$ . Transitions between energy levels of the same atom at a given ionization level, with the same principal quantum number and different total angular momentum  $J$ , have an energy difference proportional to  $\alpha^4$ . These groups of transitions are called fine-structure multiplets. Savedoff (1956) first realized that the fine structure of these energy levels could be used to break the degeneracy between the redshift effect and a possible variation of  $\alpha$ .

The value of the fine-structure constant can be measured through the separation between absorption or emission multiplets in the spectra of distant quasars (Uzan 2003) as

$$\frac{\Delta\alpha}{\alpha}(z) \equiv \frac{1}{2} \left\{ \frac{[(\lambda_2 - \lambda_1)/(\lambda_2 + \lambda_1)]_z}{[(\lambda_2 - \lambda_1)/(\lambda_2 + \lambda_1)]_0} - 1 \right\}, \quad (1)$$

where  $\lambda_{1,2}$  ( $\lambda_2 > \lambda_1$ ) are the wavelengths of the transitions and subscript 0 and  $z$  stand for their value at redshift zero (theoretical/laboratory values) and at redshift  $z$ , respectively. For illustrative purposes, expression (1) can be approximated by

$$\frac{\Delta\alpha}{\alpha} \approx \frac{\epsilon}{2\delta\lambda_0}, \quad (2)$$

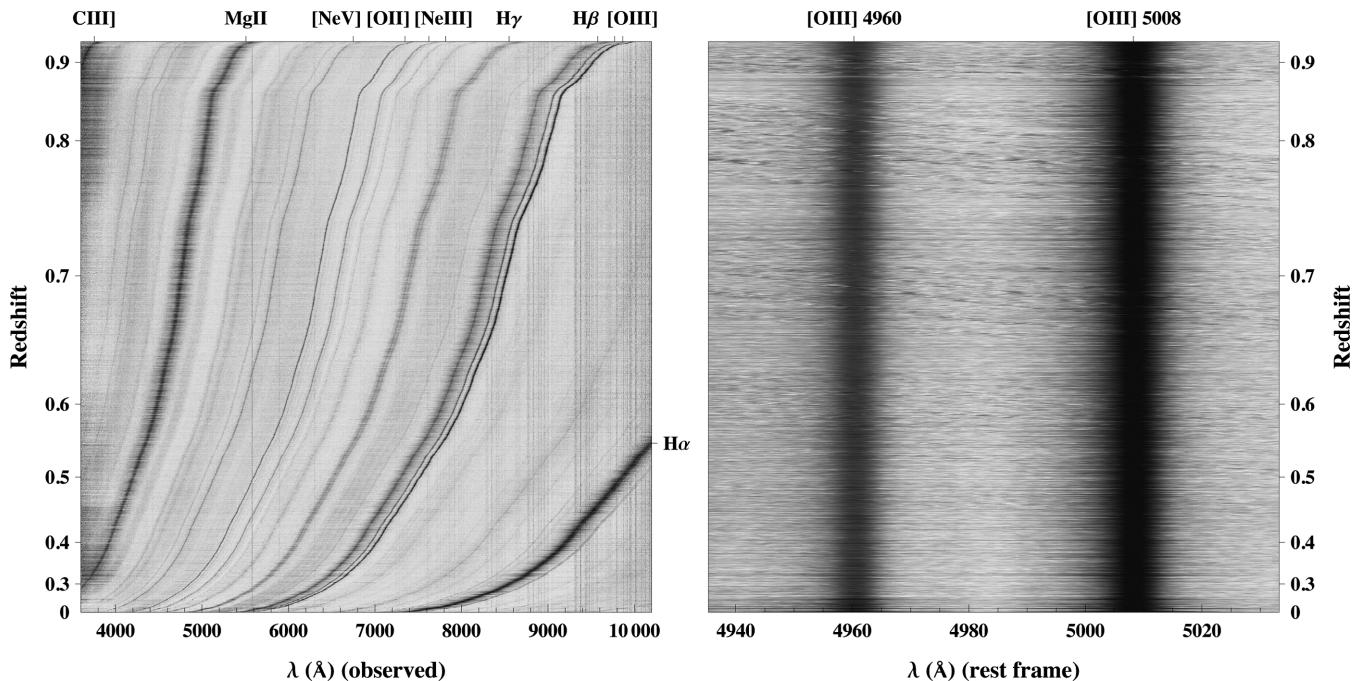


**Figure 3.** Composite image with our fiducial sample of 10 363 BOSS quasar spectra sorted by redshift. Left-hand panel: the whole range of wavelengths is shown. From right to left, the strongest emission lines are H  $\alpha$  6565 Å; [O III]  $\lambda\lambda$  4960, 5008 Å; H  $\beta$  4861 Å; H  $\gamma$  4341 Å; [Ne III]  $\lambda\lambda$  3869, 3968 Å; [O II] 3730 Å; [Ne V] 3426 Å; Mg II 2796 Å and C III] 1906 Å. The narrow straight line at 5579 Å is the strong [O I] atmospheric line. Right-hand panel: wavelength interval centred at the [O III] doublet in rest frame.

where  $\delta\lambda_0 = [\lambda_2 - \lambda_1]_0$  is the local  $z = 0$  separation between both wavelengths, and  $\epsilon = \delta\lambda_z / (1 + z) - \delta\lambda_0$  is the difference between the measured line separation at redshift  $z$  in rest frame and the local one. Thus, in principle, the larger the difference between the pair of lines, the better the precision for measuring  $\Delta\alpha/\alpha$ .

Concerning emission lines, the most suitable pair of lines is the [O III] doublet, which is often present in quasar spectra with relatively high-S/N. The vacuum values for the [O III] doublet wavelengths are

$$\lambda_1^{[\text{O III}]} = 4960.295 \text{ \AA} \quad \lambda_2^{[\text{O III}]} = 5008.240 \text{ \AA} \quad (3)$$

$$\delta\lambda_0^{[\text{O III}]} = 47.945 \text{ \AA}, \quad (4)$$

which are published in the NIST Atomic Spectra Database.<sup>1</sup> These transitions are forbidden (they correspond to magnetic dipole and electric quadrupole transitions), and they are not observed in the laboratory. The wavelength experimental values are obtained indirectly by first computing the energy levels from observed wavelengths using a theta-pinch discharge (Pettersson 1982). The wavelength separation has directly been measured in the infrared from H II regions using a balloon-borne telescope and Michelson interferometer (Moorwood et al. 1980). Both measurements of the wavelength separation, indirectly with the theta-pinch discharge and directly with the Michelson interferometer, are in good agreement, being the Michelson interferometer more accurate with an error  $< 5 \times 10^{-4}$  Å.

From equation (2), a determination of  $\epsilon$  with a precision of 1 Å allows for an uncertainty of  $10^{-2}$  in  $\Delta\alpha/\alpha$  when using the [O III] doublet. The precision from the NIST atomic data allows for a determination of  $\Delta\alpha/\alpha$  up to  $10^{-5}$ , which is a bit less than the

uncertainty in our result. One could perform a blind analysis in order to search for a possible variation on  $\alpha$ , where the absolute wavelength values are not required, if one had a large enough sample distributed in redshift. However, the precision on the absolute wavelengths limits the usefulness of high-resolution spectroscopy until better measurements of the [O III] lines (or just their separation) are available.

### 3.2 Implementation

The code developed for the analysis of the quasar spectra follows the one described in Gutiérrez & López-Corredoira (2010), although there are some modifications and more information has been extracted from the analysis. We describe the main characteristics of our code below.

#### 3.2.1 Wavelength sampling

We consider only the experimental data together with their errors as processed by the SDSS pipeline to obtain the constraint on the possible variation of  $\alpha$ . We do not resample the wavelength range by using an interpolation method. Since the pixel spacing is uniform in log-wavelengths, a given range of wavelengths in rest frame ( $\lambda_-$ ,  $\lambda_+$ ) has the same number of pixels  $N$ , i.e.

$$N \propto \int_{\lambda_- (1+z)}^{\lambda_+ (1+z)} d(\log \lambda) = \log \frac{\lambda_+ (1+z)}{\lambda_- (1+z)} = \log \frac{\lambda_+}{\lambda_-}, \quad (5)$$

and is independent of the redshift of the object. All the wavelength intervals with the same width in rest frame will have the same number of experimental points.

<sup>1</sup> [http://physics.nist.gov/PhysRefData/ASD/lines\\_form.html](http://physics.nist.gov/PhysRefData/ASD/lines_form.html)

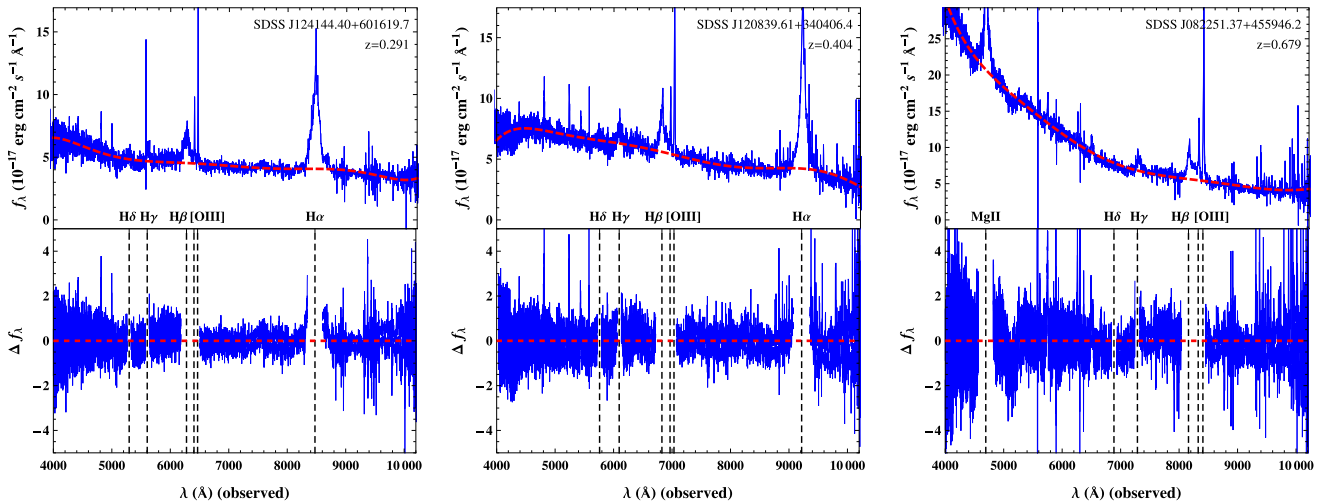


**Figure 4.** Seventh-order polynomial fits (red) to the continuum spectrum with their residuals for three typical quasar spectra at different redshift. The gaps in the residuals are the masked regions corresponding to (from right to left) H $\alpha$ , the [O III] doublet, H $\beta$ , H $\gamma$ , H $\delta$  and Mg II (black dashed lines).

### 3.2.2 Fit of the continuum spectrum

First, we fit a seventh-order polynomial to subtract the continuum spectrum while masking regions where strong and wide emission lines are present (H $\alpha$ , H $\beta$ , H $\gamma$ , H $\delta$ , Mg II and the [O III] doublet). Our method differs from Gutiérrez & López-Corredoira (2010) in that they use a cubic local spline to fit the continuum masking strong emission lines. The chosen order of the polynomial provides enough degrees of freedom to reproduce different continuum features. In Section 3, we test how our measurement for  $\Delta\alpha/\alpha$  is affected by changing the polynomial order. Hundreds of continuum spectra fits were checked by eye. The residuals from the fits are smaller than the errors on the flux densities. Fig. 4 shows three different spectra with their continuum fit and residuals.

### 3.2.3 Signal-to-noise ratio

We follow Gutiérrez & López-Corredoira (2010) for the determination of S/N. Hence, we compute the standard deviation of the flux between  $5040(1+z)$  and  $5100(1+z)$  Å (where  $z$  is the redshift of the quasar) where there are no strong emission or absorption lines. Then, we search for the maximum of the [O III] 5008 line, and determine  $S/N_{[\text{O III}]5008}$  as the ratio between the maximum of the line and the previously computed standard deviation. Although for a more reliable determination of the S/N, it is better to use a Gaussian fit to the line. This procedure avoids possible issues related when fitting data with very low S/N. This S/N is used in the criterion ii (Section 2) to build our fiducial sample.

### 3.2.4 Measurement of the emission-line wavelengths

To measure the wavelengths of the [O III] doublet, our fitting code needs as input an accurate estimate of the redshift of the quasar, at least with an error  $\Delta z < 3 \times 10^{-3}$ . This allows a search for the emission lines in a  $15 \text{ \AA}$  window around the expected location of the [O III] lines. The SDSS pipeline provides a determination of the redshift based on a  $\chi^2$  fit to different templates; we refer to Bolton et al. (2012) for more details. These redshift estimates have errors between  $10^{-4}$  and  $10^{-5}$ , which are sufficient for our purposes. Moreover, there is also a visual redshift estimation which can be found in the quasar catalogue DR12Q (Paris et al., in preparation).

The difference between both redshift estimates (if any) is usually  $|z_{\text{vis}} - z_{\text{pipe}}| \approx 5 \times 10^{-4}$ . We decided to adopt the visual redshifts.

The centroid positions of the [O III] emission lines are determined by four different methods.

#### (i) Gaussian profile method.

First, we search for the maximum flux value in an  $\sim 15(1+z)$  Å window around the expected position of the line (according to the redshift provided by the DR12Q catalogue). This procedure automatically erases any bias produced by the redshift value. Then, we make an initial Gaussian fit around the position of the maximum flux value using a fixed width of  $\sim 10(1+z)$  Å. From this first fit, we obtain a new position for the line centroid and a Gaussian width. These values are used as initial parameters for the final fit of the lines; namely, the wavelength range considered to perform the final fit is centred around the position of the line centroid, and it is four times the Gaussian width of the lines. This approach means that we consider pixels up to  $2\sigma$  away from the centre of the line. Hence, some lines are fitted using  $\sim 4$ – $5$  pixels, while others with  $\sim 15$ – $20$  pixels depending on the line width. The fit takes into account the flux errors for each pixel, i.e. we use the *ivar* column found in each spectrum as weights for the fit. Our final centroid measurement for each considered line corresponds to the centroid of the Gaussian fit done in the last step of the adopted procedure. We also derive an error for  $\Delta\alpha/\alpha$  using the standard errors for the centre position of the Gaussians. This is our main method for measuring  $\alpha$ .

#### (ii) Voigt profile method.

Following the same procedure than when using a Gaussian profile, we make the fit with a Voigt profile instead of a Gaussian. More precisely, we use a pseudo-Voigt profile which is a linear combination of a Gaussian and a Lorentzian profile. Then, we have one more parameter, i.e. the amplitude of the Lorentzian function, while its width and its position are the same as those for the Gaussian profile. In Fig. 5, we depict the [O III] and [Ne III] lines for the same quasar spectrum to illustrate the Gaussian and Voigt fitting methods.

#### (iii) Integration method.

Here, the centroids of the lines are obtained by integrating around  $1\sigma$  from the position of the fitted Gaussian profile. This technique provides indications of whether there is H $\beta$  contamination. However, due to the mid-resolution of the spectra  $R \approx 2000$ , this method is not very accurate.

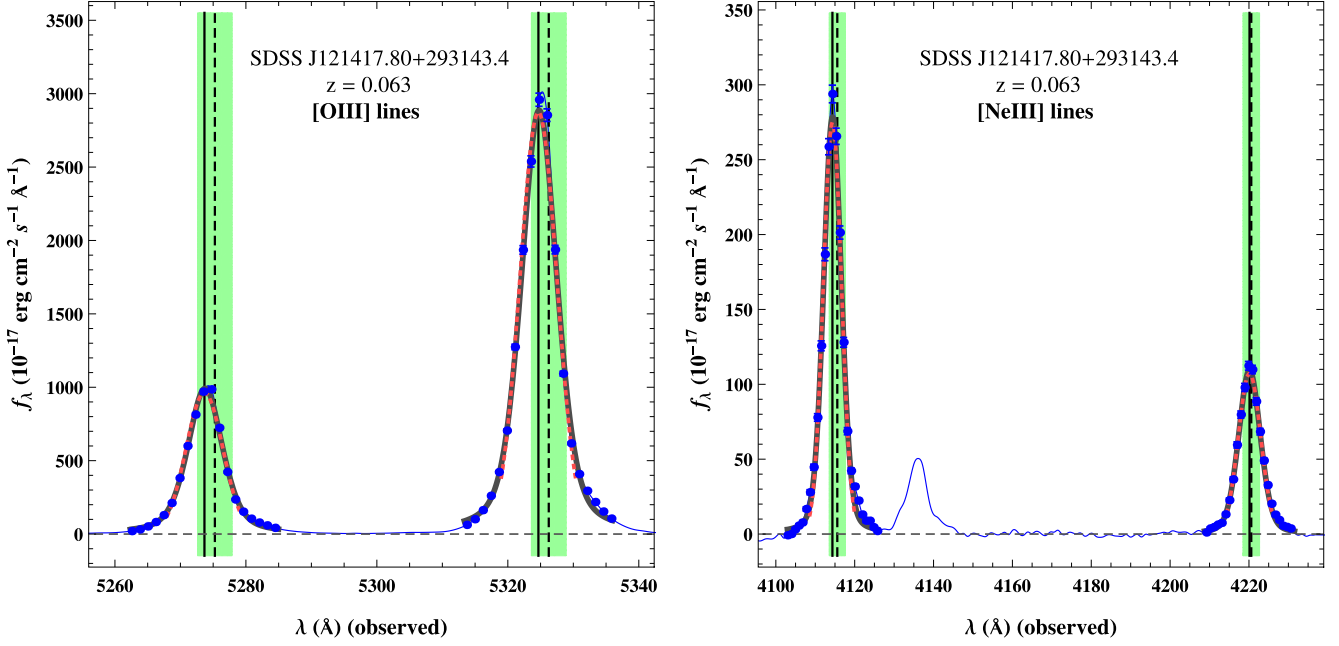


**Figure 5.** [O III] (left-hand panel) and [Ne III] (right-hand panel) lines for SDSS-J121417.80+293143.4, at redshift  $z = 0.063$ . The measured  $\Delta\alpha/\alpha$  for this quasar is  $\Delta\alpha/\alpha_{[\text{O III}]}^{\text{Gauss}} = (2.3 \pm 7.6) \times 10^{-4}$ ,  $\Delta\alpha/\alpha_{[\text{O III}]}^{\text{Voigt}} = (3.3 \pm 12.6) \times 10^{-4}$  and  $\Delta\alpha/\alpha_{[\text{Ne III}]}^{\text{Gauss}} = (39 \pm 8) \times 10^{-4}$ ,  $\Delta\alpha/\alpha_{[\text{Ne III}]}^{\text{Voigt}} = (37 \pm 9) \times 10^{-4}$ . The measured  $\Delta\alpha/\alpha$  for [Ne III] is not consistent with zero regardless of the profile; see Fig. 14 and last paragraph of Section 4 for discussion. Each panel shows the flux density for each pixel with their respective error bars (solid symbols), together with the Gaussian fit (dotted red curve) and the pseudo-Voigt profile (thick grey curve) to each of the lines. The fitting procedure (described in the text) only takes into account the experimental data (solid symbols) weighted by their error bars. Notice how the deviation of the line centroid position derived from our Gaussian fit (vertical solid line) with respect to the expected position of the line (vertical dashed line) according to the visual redshift provided by the DR12Q catalogue are well correlated for the same pair of [O III] and [Ne III] lines, and for the different set of lines. The green shaded vertical areas highlight the uncertainty for the expected position of the lines due to the quasar redshift error ( $\approx 5 \times 10^{-4}$ ). Also shown is a fourth-order spline interpolation to the spectrum after subtracting the continuum (thin solid line). The [Ne III] lines are weaker by one order of magnitude than the [O III] lines, which is usually the case for all the spectra showing both pair of lines. The weak line near the stronger [Ne III] line is blended with He I (3889.75 Å) and H  $\zeta$  (3890.16 Å).

#### (iv) Modified Bahcall method.

In Bahcall et al. (2004) the authors used a different approach to compute the line positions. They performed a third-order spline interpolation to the stronger [O III] 5008 line, then fitted this interpolation to the weaker 4960 line by adjusting the amplitude and separation of the profile. We have modified this method by using a Gaussian fit to the stronger line rather than a third-order spline.

Although we have described four different methods, the main results for  $\Delta\alpha/\alpha$  presented in this work are based on the Gaussian fitting method, while the other three are used only for comparison (see Section 4).

Finally, our final result for  $\Delta\alpha/\alpha$  and its error is obtained in the same way as in Chand et al. (2005), namely we compute a weighted mean and a weighted standard deviation, where the errors for  $\Delta\alpha/\alpha$  of each spectrum are used as weights.

### 3.3 Simulated spectra

In order to test the robustness and accuracy of our methodology, we generate realizations of quasar spectra using as noise a normal distribution centred at the flux value, and taking the error in each pixel as the standard deviation. From our fiducial sample (10 363 quasars), we simulate 100 realizations of each spectrum (> a million in total). This number of realizations provides reasonable statistics to derive an error from the standard deviation of the measurements on the realizations of each real spectrum, while the computation time remains reasonable ( $\sim 2$  d) using a standard-size computer. The es-

timated error derived from the simulations  $\Delta(\Delta\alpha/\alpha)_{\text{sim}}$  includes

$$\Delta(\Delta\alpha/\alpha)_{\text{sim}}^2 = \Delta(\Delta\alpha/\alpha)_{\text{fit}}^2 + \Delta(\Delta\alpha/\alpha)_{\text{continuum}}^2 + \Delta(\Delta\alpha/\alpha)_{\text{code}}^2, \quad (6)$$

where  $\Delta(\Delta\alpha/\alpha)_{\text{fit}}$  is the error derived from the Gaussian fits, which is our error estimate for each real spectrum;  $\Delta(\Delta\alpha/\alpha)_{\text{continuum}}$  is the error from different continuum subtraction due to the Gaussian noise, and  $\Delta(\Delta\alpha/\alpha)_{\text{code}}$  is the systematic error of our code. Then, we expect  $\Delta(\Delta\alpha/\alpha)_{\text{sim}} > \Delta(\Delta\alpha/\alpha)_{\text{fit}}$  and their difference will be an indication of the continuum and systematic errors.

Fig. 6 (left-hand panel) shows the correlation between the error in  $\Delta\alpha/\alpha$  from the Gaussian fits of each real spectrum and the standard deviation for  $\Delta\alpha/\alpha$  of its 100 realizations. The standard deviations from the simulations are within a factor of 0.5–2 of the standard errors from the fits for 97 per cent (84 per cent) of the cases when both quantities are  $< 5 \times 10^{-3}$  ( $< 50 \times 10^{-3}$ ). This shows that our code and the continuum subtraction do not introduce noticeable systematic errors compared to the Gaussian fitting. However, there is a set of spectra (9 per cent of the total) for which the simulations provide much larger errors  $\Delta(\Delta\alpha/\alpha) > 0.1$ . Fig. 6 (right-hand panel) shows the errors from the simulations as a function of redshift for our fiducial sample. Red crosses stand for spectra whose Gaussian fit error  $\Delta(\Delta\alpha/\alpha)_{\text{fit}} > 5 \times 10^{-3}$  (24 per cent). The errors are distributed in two clouds of points. For the cloud with  $\Delta(\Delta\alpha/\alpha)_{\text{sim}} \sim 1$ , the virtual realizations of each spectrum seem to differ significantly from the real spectrum. Since we use the error in each pixel to build the realizations, the relative error is large for these spectra, which is an

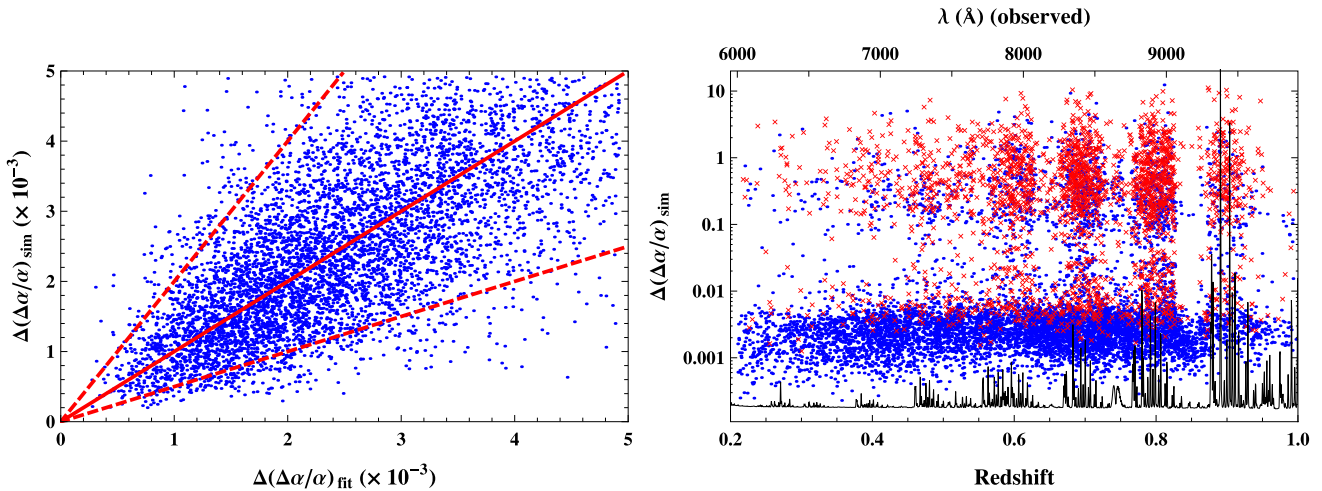


**Figure 6.** Left-hand panel: errors for  $\Delta\alpha/\alpha$  obtained from the simulations (standard deviation of the  $\Delta\alpha/\alpha$  measurements on 100 realizations of each real spectrum) and standard errors from the Gaussian fits for our fiducial sample. The solid line represents a one-to-one correspondence, while the dashed lines have slopes of 2 and 0.5. Only the simulation and fit errors smaller than  $<5 \times 10^{-3}$  are shown. Right-hand panel: errors estimated from the simulations as a function of redshift. Spectra with  $\Delta(\Delta\alpha/\alpha)_{\text{fit}} > 5 \times 10^{-3}$  are shown as red crosses (24 per cent of the total). There is a clear division between two different set of spectra which correlates with the sky emission lines (see discussion in the main text).

indication of a low S/N ratio or large absolute errors in the pixels, for instance in wavelength regions with sky emission lines. In fact, the cloud with bigger errors mimics the sky spectrum. Note also the strong correlation between this cloud of points and the spectra with large Gaussian fitting errors (red crosses). The other set of points with  $\Delta(\Delta\alpha/\alpha)_{\text{sim}} \sim 10^{-3}$  are close to our error estimation on the measurement of  $\Delta\alpha/\alpha$  based on the Gaussian fits.

As a further proof, we also simulate realizations of the 1416 dropped spectra because of sky emission lines (criterion iv, see Section 2). We found that more than 80 per cent of the spectra have  $\Delta(\Delta\alpha/\alpha)_{\text{sim}} > 0.1$ . This confirms that these spectra have very low S/N and/or large pixels error due to the proximity of the lines to strong sky emission lines.

### 3.4 Gaussian versus Voigt fitting profiles

The results obtained when using Voigt profiles instead of Gaussian ones are compared in Fig. 7. The Voigt and Gaussian measurements are  $1\sigma$ -compatible for the 93.5 per cent of the cases (98.3 per cent

at  $2\sigma$ ). Regarding the errors, there is no clear improvement when using either of both methods. However, Voigt profiles have one more parameter and restrict the number of degrees of freedom. Due to the spectral mid-resolution and the fact that the [O III] lines are very narrow, there are often only a few pixels to fit, which frequently lead to non-convergent fits. This reduces the quasar sample in  $\approx 1000$  quasars. Further discussion about both profiles can be found in Section 4.

## 4 SYSTEMATICS

In this section, we examine the possible unnoticed systematic errors by analysing different quasar samples. Table 2 summarizes all the samples considered together with their mean redshifts and the measured value for  $\Delta\alpha/\alpha$ .

We consider the following sources of systematic errors.

(i) Misidentification of the lines. The expected line widths and amplitudes are useful to avoid misidentification of the

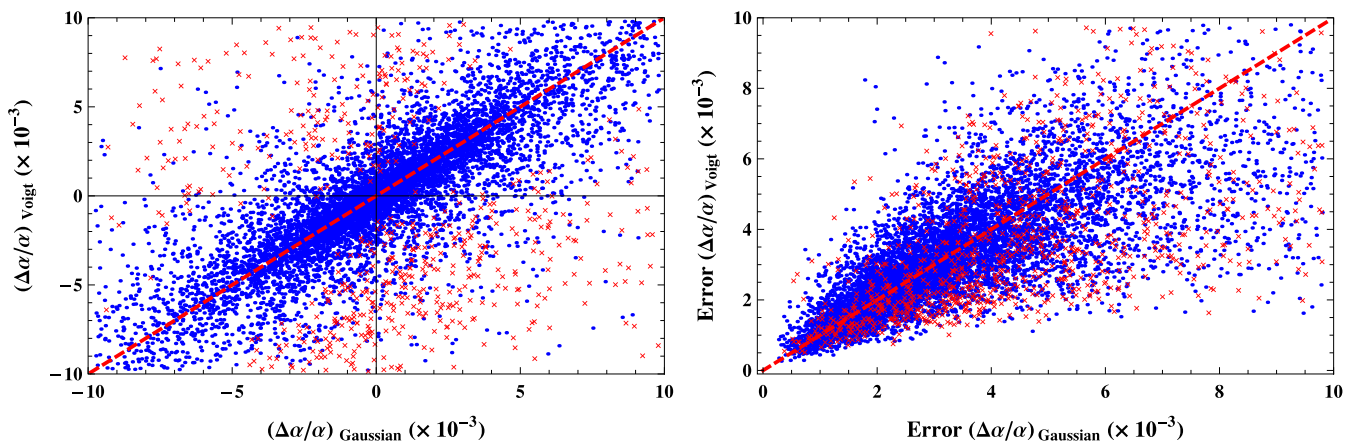


**Figure 7.** Left-hand panel: measurements of  $\Delta\alpha/\alpha$  using Gaussian and Voigt fitting profiles. Non-compatible measurements at  $1\sigma$  are shown as red crosses (6.5 per cent of the total). Right-hand panel: errors from the Gaussian and Voigt fitting. Non-compatible measurements at  $1\sigma$  are shown as red crosses.

**Table 2.** Results for  $\Delta\alpha/\alpha$  considering several samples with different constraints. The number of quasar spectra, the mean and standard deviation of the redshift and the value for  $\Delta\alpha/\alpha$  are shown.

| $\sigma_{4960/5008} - 1$                | No. of quasar spectra | Redshift        | $\Delta\alpha/\alpha (\times 10^{-5})$ |
|---|-----------------------|-----------------|--|
| <50 per cent                            | 10028                 | $0.56 \pm 0.21$ | $1.6 \pm 2.3$                          |
| <25 per cent                            | 8877                  | $0.56 \pm 0.21$ | $1.9 \pm 2.3$                          |
| <10 per cent                            | 5846                  | $0.56 \pm 0.21$ | $1.7 \pm 2.5$                          |
| <5 per cent                             | 3458                  | $0.54 \pm 0.22$ | $-0.9 \pm 3.0$                         |
| $[F_\lambda \times \sigma]_{5008/4960}$ | No. of quasar spectra | Redshift        | $\Delta\alpha/\alpha (\times 10^{-5})$ |
| $2.98 \pm 0.50$                         | 8327                  | $0.56 \pm 0.21$ | $1.8 \pm 2.4$                          |
| $2.98 \pm 0.25$                         | 5761                  | $0.55 \pm 0.21$ | $-0.4 \pm 2.6$                         |
| $2.98 \pm 0.10$                         | 2658                  | $0.54 \pm 0.21$ | $0.0 \pm 3.4$                          |
| $2.98 \pm 0.05$                         | 1411                  | $0.52 \pm 0.22$ | $5.2 \pm 4.6$                          |
| Fit width                               | No. of quasar spectra | Redshift        | $\Delta\alpha/\alpha (\times 10^{-5})$ |
| $2\sigma$                               | 10363                 | $0.56 \pm 0.21$ | $1.4 \pm 2.3$                          |
| $3\sigma$                               | 10252                 | $0.59 \pm 0.20$ | $5.5 \pm 2.5$                          |
| $4\sigma$                               | 9978                  | $0.59 \pm 0.20$ | $7.1 \pm 2.7$                          |
| $5\sigma$                               | 9726                  | $0.59 \pm 0.20$ | $5.3 \pm 2.6$                          |
| $S/N_{H\beta/[OIII]4960}$               | No. of quasar spectra | Redshift        | $\Delta\alpha/\alpha (\times 10^{-5})$ |
| <5                                      | 10338                 | $0.57 \pm 0.21$ | $1.4 \pm 2.3$                          |
| <2                                      | 9831                  | $0.57 \pm 0.21$ | $0.6 \pm 2.3$                          |
| <1                                      | 8162                  | $0.57 \pm 0.21$ | $0.1 \pm 2.5$                          |
| <0.5                                    | 5831                  | $0.58 \pm 0.21$ | $-0.7 \pm 2.8$                         |
| Pol. order (cont.)                      | No. of quasar spectra | Redshift        | $\Delta\alpha/\alpha (\times 10^{-5})$ |
| 3                                       | 10528                 | $0.57 \pm 0.21$ | $1.0 \pm 2.3$                          |
| 5                                       | 10550                 | $0.57 \pm 0.21$ | $1.3 \pm 2.3$                          |
| 7                                       | 10363                 | $0.56 \pm 0.21$ | $1.4 \pm 2.3$                          |
| 9                                       | 10471                 | $0.56 \pm 0.21$ | $-1.1 \pm 2.3$                         |
| $R^2$ (both fits)                       | No. of quasar spectra | Redshift        | $\Delta\alpha/\alpha (\times 10^{-5})$ |
| >0.9                                    | 9254                  | $0.56 \pm 0.21$ | $1.5 \pm 2.4$                          |
| >0.97                                   | 6045                  | $0.56 \pm 0.21$ | $2.8 \pm 2.7$                          |
| >0.99                                   | 2301                  | $0.54 \pm 0.21$ | $2.0 \pm 3.5$                          |
| >0.995                                  | 845                   | $0.51 \pm 0.22$ | $-0.4 \pm 4.8$                         |
| $[O III]_{5008}$ (km s <sup>-1</sup> )  | No. of quasar spectra | Redshift        | $\Delta\alpha/\alpha (\times 10^{-5})$ |
| <1000                                   | 10353                 | $0.56 \pm 0.21$ | $1.4 \pm 2.3$                          |
| <500                                    | 8990                  | $0.56 \pm 0.21$ | $0.2 \pm 2.4$                          |
| <300                                    | 2798                  | $0.52 \pm 0.22$ | $-6.8 \pm 3.9$                         |
| <200                                    | 150                   | $0.52 \pm 0.24$ | $21 \pm 18$                            |
| Method                                  | No. of quasar spectra | Redshift        | $\Delta\alpha/\alpha (\times 10^{-5})$ |
| Gaussian (weighted)                     | 4537                  | $0.58 \pm 0.20$ | $-0.4 \pm 2.8$                         |
| Gaussian                                | 4537                  | $0.58 \pm 0.20$ | $1.2 \pm 4.5$                          |
| Integration                             | 4537                  | $0.58 \pm 0.20$ | $3.6 \pm 4.8$                          |
| Modified Bahcall                        | 4537                  | $0.58 \pm 0.20$ | $0.8 \pm 4.4$                          |
| Median                                  | 4537                  | $0.58 \pm 0.20$ | $1.8 \pm 1.4$                          |
| Gauss versus Voigt                      | No. of quasar spectra | Redshift        | $\Delta\alpha/\alpha (\times 10^{-5})$ |
| Gaussian profiles                       | 8485                  | $0.55 \pm 0.19$ | $0.4 \pm 2.5$                          |
| Voigt profiles                          | 8485                  | $0.55 \pm 0.19$ | $-1.1 \pm 2.8$                         |
| Mixed profiles                          | 8485                  | $0.55 \pm 0.19$ | $1.3 \pm 2.4$                          |

[O III] emission lines. (a) Line widths: since both lines originate on the same upper energy level, their width must coincide. We check that this is the case by considering quasars whose [O III] line widths are the same within a relative fraction. For more than half of our fiducial sample, the [O III] line widths differ by less than 10 per cent (see Table 2). (b) Amplitude ratio: atomic physics states that the am-

plitude ratio between the [O III] 5008 and [O III] 4960 lines is 2.98 (Storey & Zeippen 2000, as quoted in Section 5, we obtain  $2.96 \pm 0.02_{\text{sys}}$ ). Thus, we consider different samples where this ratio differs by less than a certain amount from 2.98 (see Table 2). All the samples considered in this test yield results for  $\Delta\alpha/\alpha$  compatible with zero. Fig. 8 displays the Gaussian widths and fluxes of both [O III] emission lines for our fiducial sample.

(ii) Windows for the Gaussian fits. We use a wavelength range of  $2\sigma$  around each [O III] line in order to obtain the final Gaussian fit to the line profiles. We study how our results depend on this choice. By considering a larger wavelength interval, the results are more affected by the H  $\beta$  contamination and possible asymmetries on the line wings. The differences in the number of spectra for these samples [which are obtained by applying the selection criteria (i)–(iv) discussed in Section 2.1] arise because of the criteria concerning the non-converging fits and the sky emission lines described in Section 2.

(iii) H  $\beta$  contamination. We analyse samples where the ratio between  $S/N_{H\beta}$  and  $S/N_{[OIII]4960}$  is constrained. Despite the fact that the value for  $\Delta\alpha/\alpha$  decreases as we place more stringent constraints on H  $\beta$ , it is always consistent with no variation in  $\alpha$  within the errors. This analysis demonstrates that the strength and/or width of the H  $\beta$  line do not affect substantially the result for  $\Delta\alpha/\alpha$  when a weighted mean is adopted.

(iv) Continuum subtraction. We use a seventh-order polynomial to subtract the continuum spectrum. We examine if the polynomial order has important effects on our measurements. Our values for  $\Delta\alpha/\alpha$  and their errors are only slightly affected by the chosen polynomial order.

(v) Goodness of Gaussian fits. We quantify the quality of the Gaussian fits by the  $R^2$  coefficient. All the considered samples show values for  $\Delta\alpha/\alpha$  consistent with no variation in  $\alpha$ .

(vi) Broad lines. We also study samples where the width of both lines is less than a certain value (in km s<sup>-1</sup>). These samples are consistent with no variation of  $\alpha$ . Samples built from narrow lines <300 km s<sup>-1</sup> may be more affected by misidentification of [O III] lines as sky lines.

(vii) Different methods for measuring the [O III] line position. We compare the results obtained by the methods to measure the position of the [O III] lines described in Section 3.2.4. Since not all the methods provide an error for the measurement, we cannot calculate a weighted mean, and it is necessary to select a more restricted sample. Then, we consider a sample where the difference between the widths of the lines is less than 25 per cent, the amplitude ratio is constrained to differ from the theoretical value 2.98 (Storey & Zeippen 2000) by less than 0.5, and the  $S/N_{H\beta}$  is smaller than half the  $S/N_{[OIII]4960}$ .

(viii) Gaussian versus Voigt profiles. We compare the results for 8485 quasars from our fiducial sample after dropping 1878 spectra with non-converging Voigt fits (this reduction increases the statistical error). We also compute a ‘mixed’ value for  $\Delta\alpha/\alpha$  where for each spectrum we use the value for the variation of the fine-structure constant with smaller error, either  $(\Delta\alpha/\alpha)_{\text{Gauss}}$  or  $(\Delta\alpha/\alpha)_{\text{Voigt}}$ .

We have also analysed the standard deviation and errors of the results for  $\Delta\alpha/\alpha$  as a function of redshift (Fig. 9). Even though we have imposed a constraint on our initial sample based on the sky emission lines, the standard deviation and errors still correlate with the sky. In particular, for the correlation with the moving standard deviation, this means that the precision in our measurement of  $\Delta\alpha/\alpha$  along the whole redshift interval is limited by the sky subtraction algorithm.

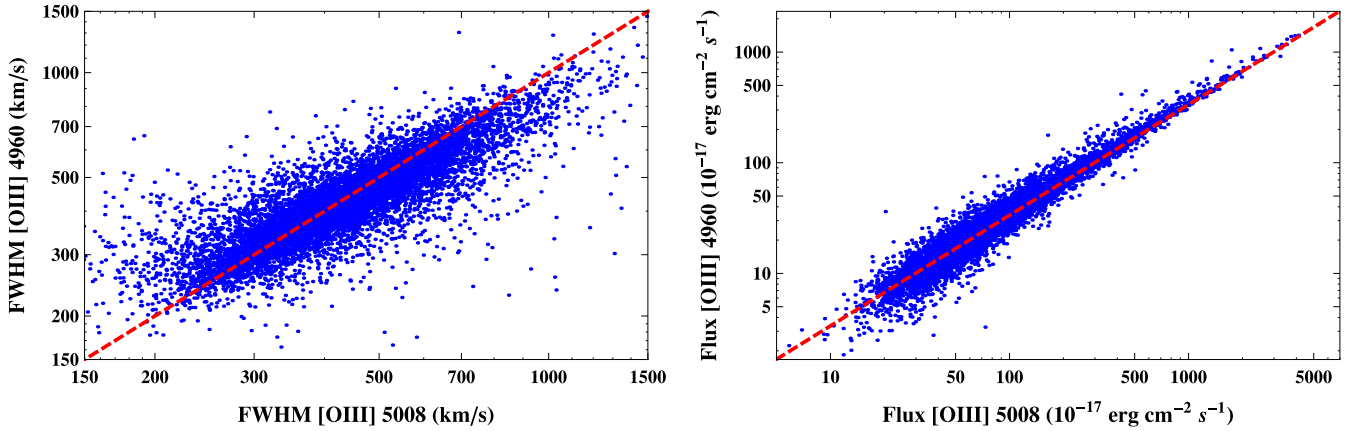


**Figure 8.** Left-hand panel: Gaussian widths (in  $\text{km s}^{-1}$ ) for both [O III] lines. Both lines originate on the same upper energy level, then their widths must coincide (red dashed line). Right-hand panel: fluxes for both [O III] lines. The theoretical flux ratio is 2.98 (red dashed line). The entire fiducial quasar sample is shown.

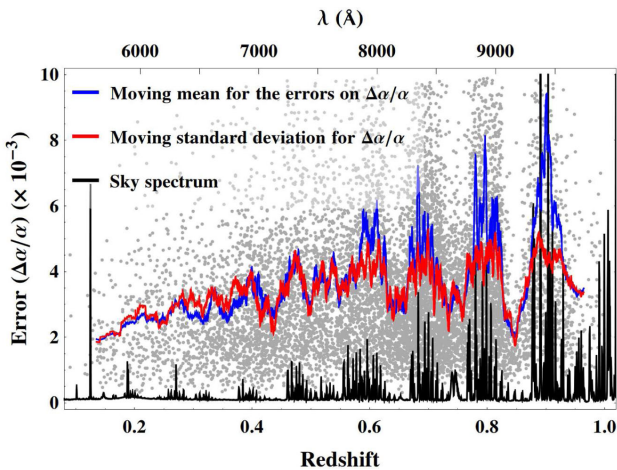


**Figure 9.** Errors for  $\Delta\alpha/\alpha$  derived from the Gaussian fits (grey points) for our fiducial sample, moving mean of the these errors (blue line) using overlapping bins (100 spectra per bin,  $\Delta z \approx 0.025$ ), moving standard deviation of  $\Delta\alpha/\alpha$  measurements using the same bins (red line) and a typical sky spectrum.

## 5 RESULTS

### 5.1 [O III] lines

We used a total of 10 363 quasar spectra, drawn from the SDSS-III/BOSS DR12Q catalogue, after applying the selection criteria (i)–(iv) (see Section 2), to measure the possible variation of the fine-structure constant. The following measurement is obtained:

$$\frac{\Delta\alpha}{\alpha} = (1.4 \pm 2.3) \times 10^{-5}.$$

This value is consistent with the previous results reported in different investigations based on the same method: Bahcall et al. (2004), Gutiérrez & López-Corredoira (2010), and Rahmani et al. (2014). The redshift dependence of the measurements is shown in Fig. 10 (left-hand panel), where several bins have been made taking into account the redshift intervals affected by the sky (shaded zones). In the right-hand panel, we show the results obtained from the simulations described in Section 3, using the same redshifts intervals for the bins. The main differences between the real results and the

simulations are in the regions where there are strong sky lines (shaded regions), while being in agreement in the remaining zones. Detailed information about each bin for the real data can be found in Table 3.

Our results are little affected by the specific constraints imposed in our sample as discussed in Section 4. For instance, we vary the width for the Gaussian fits, the contamination of H $\beta$ , the polynomial order used to fit the continuum spectrum, the quality of the Gaussian fits and test different methods to measure  $\Delta\alpha/\alpha$ . The most important effect found is that by considering broader widths for the Gaussian fits, the results are more affected by the contamination from H $\beta$  and possible asymmetries in the line wings. We have also checked for possible misidentifications of the [O III] emission lines using their expected widths and amplitude ratio.

Table 4 contains the results for  $\Delta\alpha/\alpha$  when the lower bound on the  $S/N_{[\text{O III}] 5008}$  is increased. All the results remain consistent with no variation of the fine-structure constant. In Fig. 11, the measured  $\Delta\alpha/\alpha$  for our fiducial sample as a function of the  $S/N_{[\text{O III}] 5008}$  are plotted together with their errors.

The distribution of BOSS quasars in the sky (see Fig. 1, left-hand panel) suggests to divide the sample into two, one for the North galactic cap and one for the South galactic cap. Table 5 describes the results for each galactic hemisphere, and no statistical meaningful difference is found. In order to look for a spatial variation, we also carried out a more precise analysis by fitting a dipole. First, we fixed the direction on the sky of the dipole and performed a linear fit ( $\Delta\alpha/\alpha(\theta) = a \cos \theta + b$ ) of the measurements of the variation of the fine-structure constant as a function of  $\cos \theta$ , where  $\theta$  is the angle between the dipole axis and a quasar in the sky. Different fits were done for the dipole axis lying in a grid in RA and Dec. ( $\sim 1^\circ \times 1^\circ$ ). However, there is not statistical significance to determine the dipole axis with a meaningful error, i.e. smaller than the whole sky. There has been a claim on a significant deviation of  $\alpha$  from being a constant as a function of space (King et al. 2012), with a dipole amplitude  $0.97^{+0.22}_{-0.20} \times 10^{-5}$  in the direction  $\text{RA} = 17.3 \pm 1.0$  h and  $\text{Dec.} = -61^\circ \pm 10^\circ$ . Fixing the dipole in that direction, we get  $(-4.3 \pm 3.4) \times 10^{-5}$  for the dipole amplitude and  $(0.8 \pm 2.3) \times 10^{-5}$  for the monopole term, which are not precise enough to compare with that work.

We are inclined to parametrize the possible time variation of  $\alpha$  with redshift  $z$ . This is justified since any possible variation on  $\alpha$  must be dominated by the local geometry of space–time (at least

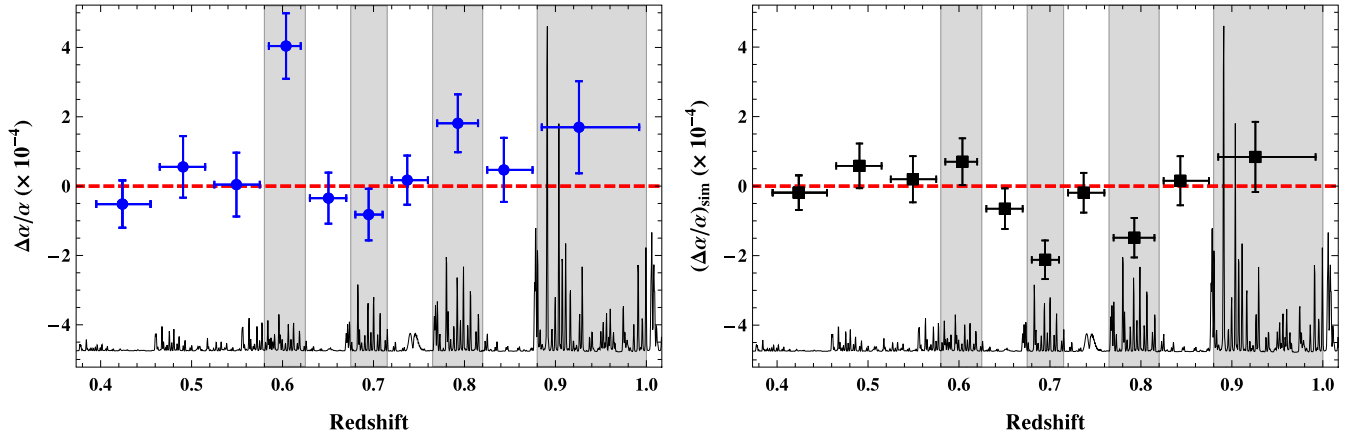


**Figure 10.** Left-hand panel:  $\Delta\alpha/\alpha$  versus redshift (real data). Details about each bin are listed in Table 3. Right-hand panel:  $(\Delta\alpha/\alpha)_{\text{sim}}$  versus redshift (simulations). A typical sky spectrum and shadowed regions where the sky contamination is expected to be large, are shown as reference.

**Table 3.** Detailed information about the bins in Fig. 10.

| Redshift interval | No. of quasar spectra | Redshift        | $\Delta\alpha/\alpha (\times 10^{-5})$ |
|-------------------|-----------------------|-----------------|--|
| 0.390–0.460       | 817                   | $0.42 \pm 0.02$ | $-5.2 \pm 6.8$                         |
| 0.460–0.520       | 723                   | $0.49 \pm 0.02$ | $5.5 \pm 8.9$                          |
| 0.520–0.580       | 757                   | $0.55 \pm 0.02$ | $0.4 \pm 9.2$                          |
| 0.580–0.625       | 843                   | $0.60 \pm 0.01$ | $40.4 \pm 9.4$                         |
| 0.625–0.675       | 988                   | $0.65 \pm 0.01$ | $-3.5 \pm 7.4$                         |
| 0.675–0.715       | 1299                  | $0.69 \pm 0.01$ | $-8.2 \pm 7.4$                         |
| 0.715–0.765       | 1117                  | $0.74 \pm 0.01$ | $1.7 \pm 7.1$                          |
| 0.765–0.820       | 1444                  | $0.79 \pm 0.02$ | $18.1 \pm 8.3$                         |
| 0.820–0.880       | 644                   | $0.84 \pm 0.02$ | $4.7 \pm 9.2$                          |
| 0.880–1.000       | 580                   | $0.93 \pm 0.03$ | $17.0 \pm 13.3$                        |

**Table 4.** Results for several samples with different constraints on the  $S/N_{[\text{O III}] 5008}$ . For each sample, the number of quasar spectra, the mean redshift, together with its standard deviation and the value for  $\Delta\alpha/\alpha$  are shown.

| $S/N_{[\text{O III}] 5008}$ | No. of quasar spectra | Redshift        | $\Delta\alpha/\alpha (\times 10^{-5})$ |
|-----------------------------|-----------------------|-----------------|--|
| >10                         | 10 363                | $0.56 \pm 0.21$ | $1.4 \pm 2.3$                          |
| >20                         | 5270                  | $0.53 \pm 0.21$ | $-0.5 \pm 2.5$                         |
| >50                         | 1498                  | $0.47 \pm 0.20$ | $-3.4 \pm 3.1$                         |
| >100                        | 451                   | $0.41 \pm 0.19$ | $-2.0 \pm 3.6$                         |
| >500                        | 12                    | $0.24 \pm 0.19$ | $6 \pm 12$                             |

if we consider the dynamics of the Universe as the main reason for such variation). Therefore, one is led to consider the possible variation of  $\alpha$  as a function of redshift ( $z = 1/a(t) - 1$ ) or the Ricci scalar ( $R(t) = 6H(t)^2[1 - q(t)]$ ), where  $a(t)$  is the scale factor,  $H(t)$  the Hubble parameter and  $q(t)$  is the deceleration parameter. Since the Ricci scalar is not known for each quasar, it is straightforward to consider a possible variation with redshift. In contrast, for a time parametrized model of the variation of  $\alpha$  the analysis depends on the particular cosmology considered. Since there is no significant clear dependence, we use a linear model in redshift. Then, for

$$\Delta\alpha/\alpha = az + b, \quad (7)$$

we obtain

$$a = (0.7 \pm 2.1) \times 10^{-4}; \quad b = (0.7 \pm 1.4) \times 10^{-4}; \quad (8)$$

which do not show any dependence of  $\Delta\alpha/\alpha$  with redshift.

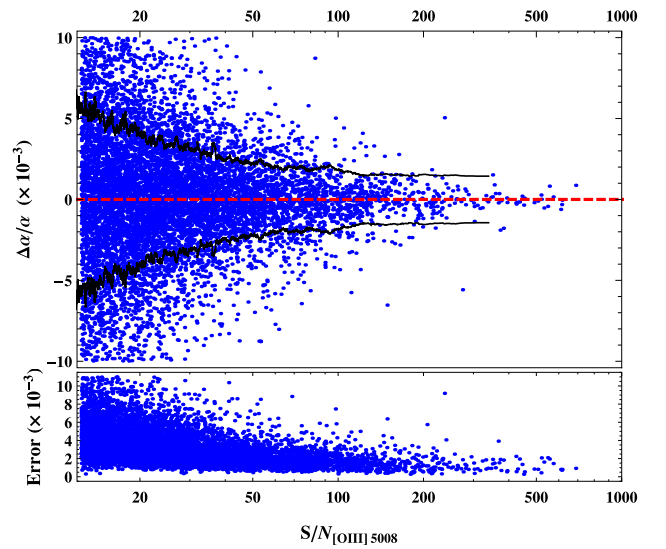


**Figure 11.**  $\Delta\alpha/\alpha$  versus  $S/N_{[\text{O III}] 5008}$  (top panel) with the moving standard deviation (black lines) using overlapping bins (100 spectra per bin) and the error on  $\Delta\alpha/\alpha$  (bottom panel) in linear-log scale for our fiducial sample. The deviation of  $\Delta\alpha/\alpha$  from zero and its error steadily decreases as the  $S/N$  increases.

**Table 5.** Results for the North and South galactic hemispheres.

| Galactic hemisphere | No. of quasar spectra | Redshift        | $\Delta\alpha/\alpha (\times 10^{-5})$ |
|---------------------|-----------------------|-----------------|--|
| North               | 8069                  | $0.56 \pm 0.21$ | $2.6 \pm 2.6$                          |
| South               | 2294                  | $0.59 \pm 0.20$ | $-3.1 \pm 4.9$                         |

From this sample, we also obtain a value for the line ratio  $[F_\lambda \times \sigma]_{5008} / [F_\lambda \times \sigma]_{4960} = 2.96 \pm 0.02_{\text{sys}}$ , where  $F_\lambda$  is the maximum flux density of the line, and  $\sigma$  is the Gaussian width. The value reported is a weighted mean where the  $S/N_{[\text{O III}] 5008}$  is used as weights. The quoted systematic error is computed from the analysis of samples with different polynomial orders for the continuum fit and different widths for the line fitting (see Table 6), since this quantity is more affected by these two parameters. The value we obtain is in agreement with the best current theoretical value, i.e. 2.98 (Storey & Zeppen 2000).

**Table 6.** Results for the line ratio when polynomials of different orders are used to subtract the continuum and different range for the Gaussian fits are used. For each sample, the number of quasar spectra, the mean redshift together with its standard deviation and the value for  $[F_\lambda \times \sigma]_{5008}/[F_\lambda \times \sigma]_{4960}$  are shown.

| Polynomial order | No. of quasar spectra | Redshift        | $[F_\lambda \times \sigma]_{5008/4960}$ |
|------------------|-----------------------|-----------------|---|
| 3                | 10 528                | $0.57 \pm 0.21$ | 2.96                                    |
| 5                | 10 550                | $0.57 \pm 0.21$ | 2.94                                    |
| 7                | 10 363                | $0.56 \pm 0.21$ | 2.96                                    |
| 9                | 10 471                | $0.56 \pm 0.21$ | 2.98                                    |
| Fit width        | No. of quasar spectra | Redshift        | $[F_\lambda \times \sigma]_{5008/4960}$ |
| $2\sigma$        | 10 363                | $0.56 \pm 0.21$ | 2.96                                    |
| $3\sigma$        | 10 252                | $0.59 \pm 0.20$ | 2.92                                    |
| $4\sigma$        | 9 978                 | $0.59 \pm 0.20$ | 2.98                                    |
| $5\sigma$        | 9 726                 | $0.56 \pm 0.21$ | 2.98                                    |

**Table 7.** Results for SDSS-II/DR7 and BOSS (SDSS-III/DR12) samples. For each sample, the number of quasar spectra, the mean redshift, together with its standard deviation and value for  $\Delta\alpha/\alpha$  are shown.

| Sample           | No. of quasar spectra | Redshift        | $\Delta\alpha/\alpha (\times 10^{-5})$ |
|------------------|-----------------------|-----------------|--|
| DR7              | 2853                  | $0.38 \pm 0.15$ | $0.5 \pm 2.8$                          |
| DR7 (SDSS cont.) | 3009                  | $0.38 \pm 0.15$ | $-0.4 \pm 2.7$                         |
| BOSS (DR12)      | 10 363                | $0.56 \pm 0.21$ | $1.4 \pm 2.3$                          |
| BOSS + DR7       | 13 175                | $0.51 \pm 0.21$ | $0.9 \pm 1.8$                          |

Finally, we have also considered quasar spectra from the SDSS-II/DR7, which were observed using the previous spectrograph instead of the upgraded BOSS spectrograph (see Section 2). From the DR7 quasar catalogue (Schneider et al. 2010), which contains 105 783 quasars, we select a sample of 2853 quasars up to redshift  $z = 0.8$  using the same criteria described in Section 2. This number is similar to the quasar spectra considered by Rahmani et al. (2014, Table 1). We re-analyse this sample using the methodology presented in this work, and we find  $\Delta\alpha/\alpha = (0.5 \pm 2.8) \times 10^{-5}$ . By combining this DR7 sample with our fiducial BOSS (DR12) quasar sample (after eliminating 41 spectra which were re-observed by BOSS), we obtain our final sample which contains a total of 13 175 quasars. The value obtained for this combined sample is reported as a final result of this investigation:

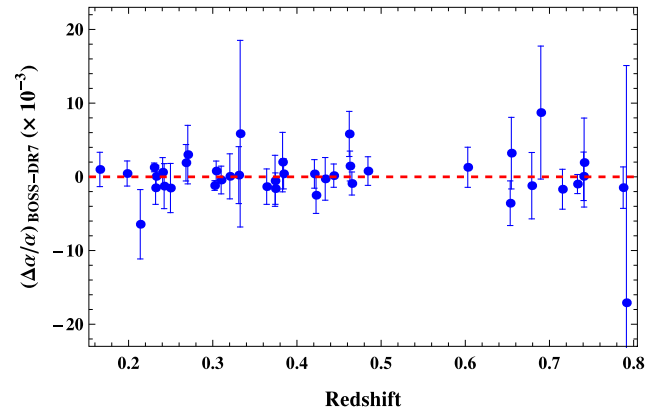
$$\frac{\Delta\alpha}{\alpha} = (0.9 \pm 1.8) \times 10^{-5}.$$

Table 7 shows the results for DR7, DR7 using the continuum fit provided by the SDSS pipeline,<sup>2</sup> BOSS (DR12) and the combined BOSS+DR7. It can be seen that the mean redshift for the DR7 sample is lower than that for BOSS. Note that there is also a big difference on the mean  $S/N_{[\text{O III}] 5008}$  of both samples:  $S/N_{[\text{O III}] 5008}^{\text{DR7}} = 60$  and  $S/N_{[\text{O III}] 5008}^{\text{BOSS}} = 33$ , which also explains why the statistical errors for  $\Delta\alpha/\alpha$  do not reflect the expected reduction due to the increase in the number of quasars of our BOSS sample. Table 8 shows the results of  $\Delta\alpha/\alpha$  using the combined sample in the same redshift bins considered for our fiducial sample. Fig. 12 shows the difference of the values obtained for  $\Delta\alpha/\alpha$  for the 41 re-observed quasars. Both BOSS and DR7 measurements are in

<sup>2</sup> The SDSS pipeline provides a continuum fit for the DR7 spectra. The good agreement between the value for  $\Delta\alpha/\alpha$  obtained with the SDSS continuum fit and our continuum fit is a good test for our code.

**Table 8.** Values of  $\Delta\alpha/\alpha$  using the combined sample BOSS+DR7 for the same redshift bins as in Table 3.

| Redshift interval | No. of quasar spectra | Redshift        | $\Delta\alpha/\alpha (\times 10^{-5})$ |
|-------------------|-----------------------|-----------------|--|
| 0.390–0.460       | 1279                  | $0.42 \pm 0.02$ | $-2.5 \pm 4.8$                         |
| 0.460–0.520       | 1076                  | $0.49 \pm 0.02$ | $7.2 \pm 6.4$                          |
| 0.520–0.580       | 1071                  | $0.55 \pm 0.02$ | $1.1 \pm 7.1$                          |
| 0.580–0.625       | 1025                  | $0.60 \pm 0.01$ | $30.8 \pm 8.1$                         |
| 0.625–0.675       | 1191                  | $0.65 \pm 0.01$ | $-5.1 \pm 6.5$                         |
| 0.675–0.715       | 1424                  | $0.69 \pm 0.01$ | $-6.2 \pm 7.0$                         |
| 0.715–0.765       | 1220                  | $0.74 \pm 0.01$ | $1.4 \pm 6.8$                          |
| 0.765–0.820       | 1519                  | $0.79 \pm 0.02$ | $15.0 \pm 8.1$                         |
| 0.820–0.880       | 644                   | $0.84 \pm 0.02$ | $4.7 \pm 9.2$                          |
| 0.880–1.000       | 580                   | $0.93 \pm 0.03$ | $17.0 \pm 13.3$                        |



**Figure 12.** Difference between  $(\Delta\alpha/\alpha)_{\text{BOSS}}$  and  $(\Delta\alpha/\alpha)_{\text{DR7}}$  measurements for the 41 quasars observed by SDSS-II/III that were re-observed by BOSS. Both values for  $\Delta\alpha/\alpha$  are consistent.

perfect agreement within the error bars. This test is a good check for the reliability of our code and the consistency of the SDSS spectra obtained with different spectrographs.

There are massive galaxy surveys to be carried out during the next decade. For instance, eBOSS and DESI will take spectra from millions of galaxies. Therefore, it is interesting to give an estimation of the accuracy that will be obtained when using galaxy spectra instead of quasars. For this, we have analysed the galaxy spectra collected by the DEEP2 survey (Newman et al. 2013) taken with resolving power  $\approx 6000$ . From this sample, we found 4056 galaxies with strong [OIII] lines. Naively, one would expect that the error on  $\Delta\alpha/\alpha$  should be

$$\Delta(\Delta\alpha/\alpha)_{\text{galaxies, DEEP2}} \approx f_{\text{sample}} \times f_{\text{inst}} \times f_{\text{object}} \times \Delta(\Delta\alpha/\alpha)_{\text{quasars, BOSS}}, \quad (9)$$

where  $f_{\text{sample}} (= \sqrt{10\,363/4056})$  takes into account the different number of objects in each sample,  $f_{\text{inst}} (\approx 2000/6000)$  stands for the different resolution of the spectra and  $f_{\text{object}}$  is an extra factor due to the different characteristics of quasar and galaxy emission lines which affect the uncertainty of the line positions. This last factor is proportional to the line widths and inversely proportional to the line fluxes:

$$f_{\text{object}} \approx \frac{\text{FWHM}_{\text{galaxies}}}{\text{FWHM}_{\text{quasars}}} \times \left( \frac{\text{Flux}_{\text{galaxies}}}{\text{Flux}_{\text{quasars}}} \right)^{-1}. \quad (10)$$

These numbers for the [O III] 5008 line are approximately  $\text{FWHM}_{\text{galaxies}} \approx 120 \text{ km s}^{-1}$ ,  $\text{FWHM}_{\text{quasars}} \approx 420 \text{ km s}^{-1}$ ,

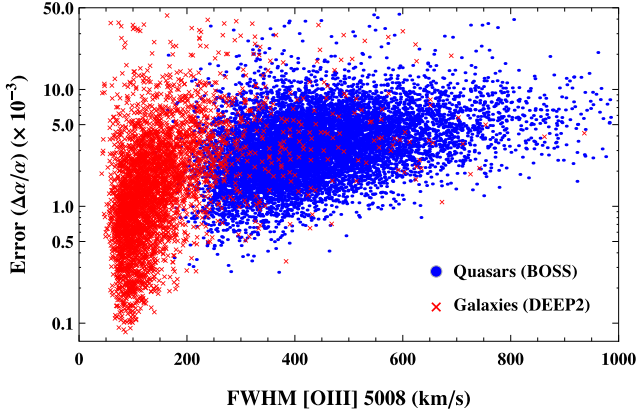


**Figure 13.** Errors on  $\Delta\alpha/\alpha$  as a function of the FWHM of [O III] 5008 for our fiducial BOSS quasar sample (blue points) and for the DEEP2 galaxy sample (red crosses).

$\text{Flux}_{\text{galaxies}} \approx 70$  and  $\text{Flux}_{\text{quasars}} \approx 210$  in units of  $10^{-17} \text{ erg cm}^{-2} \text{ s}^{-1}$ , obtained from the DEEP2 sample and from our fiducial sample. Thus, the expected error is  $1.1 \times 10^{-5}$ , where we have considered the error of our fiducial sample  $\Delta(\Delta\alpha/\alpha)_{\text{quasars, BOSS}} = 2.3 \times 10^{-5}$ . Applying the same criteria described in Section 2 to the DEEP2 galaxy sample, we get  $\Delta\alpha/\alpha = (-0.9 \pm 1.6) \times 10^{-5}$ . Thus, the upcoming future galaxy surveys will be quite competitive for constraining the variation of the fine-structure constant at low redshift  $z < 2$ . Fig. 13 shows the error on  $\Delta\alpha/\alpha$  for the DEEP2 and BOSS samples.

## 5.2 [Ne III] lines

We also measure from 462 quasar spectra with [Ne III] emission lines the following constraint on the fine-structure constant:

$$\Delta\alpha/\alpha_{[\text{Ne III}]} = (34 \pm 1) \times 10^{-4}, \quad (11)$$

to be compared with

$$\Delta\alpha/\alpha_{[\text{Ne III}]} = (36 \pm 1) \times 10^{-4} \quad (12)$$

obtained by Gutiérrez & López-Corredoira (2010). The analysis of the [Ne III] lines reveals the same systematic effect previously observed, namely a clear tendency for a positive variation of  $\alpha$ . Fig. 14 compares the results obtained for  $\Delta\alpha/\alpha$  for spectra where both [O III] and [Ne III] lines are present. To account for this effect, a shift  $\sim 0.6 \text{ \AA}$  on the theoretical or observed values of the wavelengths for the [Ne III] lines is necessary. There are experimental (Bowen 1955) and indirect (Kramida & Nave 2006) values for the wavelengths of the [Ne III] lines which are in agreement with errors  $\approx 3 \times 10^{-2} \text{ \AA}$ . We use the NIST values for the [Ne III] lines

$$\lambda_1^{[\text{Ne III}]} = 3869.86 \text{ \AA} \quad \lambda_2^{[\text{Ne III}]} = 3968.59 \text{ \AA} \quad (13)$$

$$\delta\lambda_0^{[\text{Ne III}]} = 98.73 \text{ \AA}. \quad (14)$$

The results for the [O III] doublet guarantee the good calibration of the SDSS spectra (and many more independent scientific results based on the SDSS spectra). Thus, we have measured the [Ne III] lines using a high-resolution optical spectrum from the planetary nebula IC 418. The IC 418 optical spectrum (3600–7200 Å) was taken under service time at the Nordic Optical Telescope (NOT; Roque de los Muchachos, La Palma) in 2013 March with the FIES spectrograph. We used FIES in the low-resolution mode

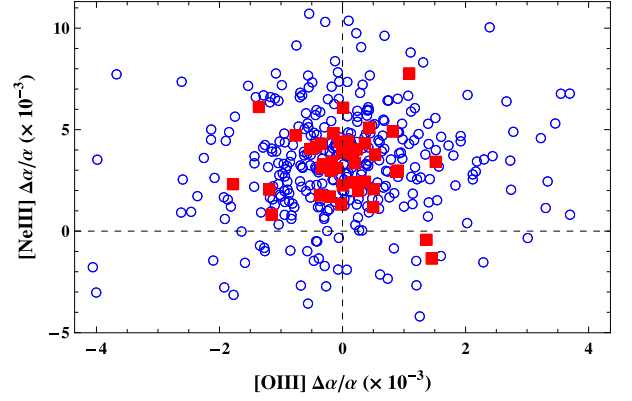


**Figure 14.** [Ne III] and [O III] measurements for  $\Delta\alpha/\alpha$ . Empty symbols stand for spectra with  $S/N_{[\text{Ne III}] 3869} < 35$  and solid squares for spectra with  $S/N_{[\text{Ne III}] 3869} > 35$ . [Ne III] measurements have a clear tendency to a positive variation of  $\alpha$ , which is due to a systematic effect affecting the [Ne III] measurement. The same effect has already been noticed by Gutiérrez & López-Corredoira (2010), and it is explained in Section 5.2.

( $R \approx 25000$ ) with the 2.5 arcsec fibre (centred at the central star of IC 418). Three exposures of 1200 s each were combined into a final IC 418 spectrum, reaching a S/N (in the stellar continuum) of  $\sim 60$  at 4000 Å and in excess of  $\sim 150$  at wavelengths longer than 5000 Å (see Díaz-Luis et al. 2015, for more observational details). To measure  $\Delta\alpha/\alpha$ , we need to know the ratio

$$\mathcal{R} = [(\lambda_2 - \lambda_1) / (\lambda_2 + \lambda_1)]_0, \quad (15)$$

which is independent of the peculiar velocity of the planetary nebula. From our data, we obtain

$$\mathcal{R} = (1259561 \pm 4) \times 10^{-8}, \quad (16)$$

compared to the one using NIST values for the wavelengths

$$\mathcal{R}_{\text{NIST}} = 1259560 \times 10^{-8}. \quad (17)$$

The difference between the two values translates into a variation on  $\Delta\alpha/\alpha < 10^{-6}$ . Thus, the measured wavelength separation for the [Ne III] doublet does not account for the positive variation on  $\alpha$  observed using these lines. Fig. 15 (left-hand panel) shows the Gaussian fit to the [Ne III] line profiles present in the IC 418 spectrum.

The IC 418 spectrum shows two different lines near the [Ne III] 3968 Å line (see Fig. 15, right-hand panel). The stronger one is H  $\epsilon$  3971 Å, the other one is He I 3965 Å. Hence, we search for a possible blending of the [Ne III] line 3968 with these two lines in our much lower spectral resolution quasar spectra. Fig. 16 (left-hand panel) shows stack quasar spectra with broad [Ne III] emission lines. It can be seen that the weak [Ne III] line is blended.

To quantify the displacement produced by the blending with H  $\epsilon$  line, we did a Gaussian convolution of the Planetary Nebula spectrum to lower the resolution down to  $R \approx 2000$ . Since the line intensity ratio of [Ne III] and H  $\epsilon$  may differ in the quasar narrow emission-line region and the Planetary Nebula, we show in Fig. 16 (right-hand panel) the shift produced by the H  $\epsilon$  line as a function of the ratio [Ne III]/H  $\epsilon$ . We get a shift  $\sim 0.6 \text{ \AA}$  when H  $\epsilon$ /[Ne III] is  $\sim 0.5$ . This explains the systematic found when using [Ne III] lines to measure the variation of the fine-structure constant  $\Delta\alpha/\alpha$  in previous studies (Gutiérrez & López-Corredoira 2010; Grupe et al. 2005).

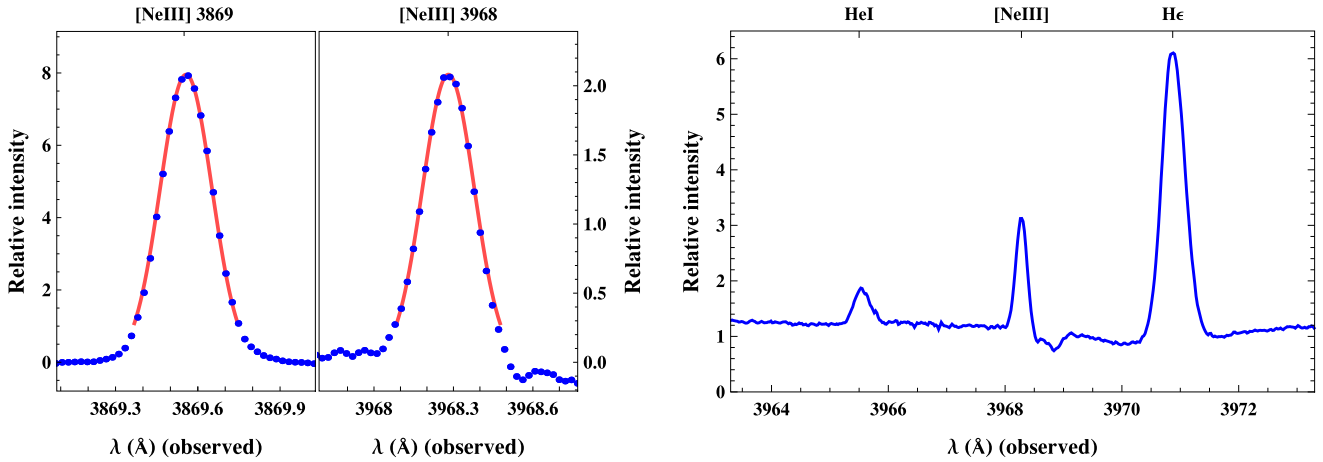


**Figure 15.** Left-hand panel: [Ne III] 3869 and [Ne III] 3968 together with our Gaussian fits (solid line) from a high-resolution ( $R \approx 25\,000$ ) spectrum of the Planetary Nebula IC 418 obtained with the FIES spectrograph at the NOT telescope. Right-hand panel: IC 418 spectrum centred at [Ne III] 3968 line. The two close lines are H  $\epsilon$  3971 Å and He I 3965 Å.

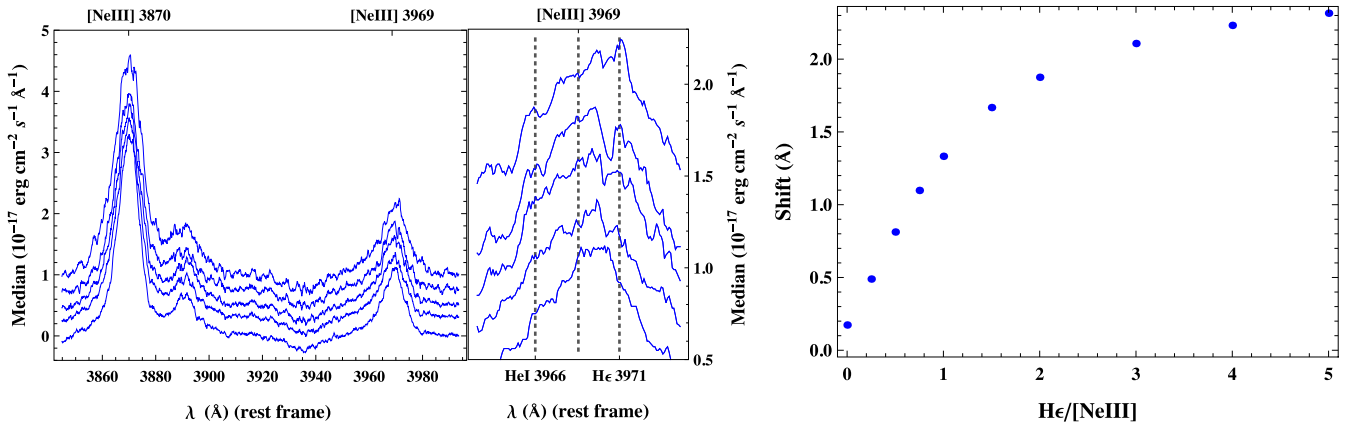


**Figure 16.** Left-hand panel: median-stacked quasar spectra with broad [Ne III] lines (increasing line width from bottom to top). Both [Ne III] lines are shown ( $\lambda\lambda$  3869, 3968 Å). The weak [Ne III] line is blended with the two lines H  $\epsilon$  3971 Å and He I 3965 Å. Right-hand panel: shift produced by the H  $\epsilon$  line in the [Ne III] 3968 line as a function of the line intensity ratio of both lines as measured from the Planetary Nebula convolved spectrum.

## 6 SUMMARY

The main conclusions of this work are as follows.

(i) From 45 802 objects at  $z < 1$  classified as quasars in the SDSS-III/BOSS DR12 quasar catalogue, we have extracted a sample of 10 363 quasars with [O III] emission lines. Combining this fiducial sample with a sample of 2853 previously studied SDSS-II/DR7 quasars, we got a final sample of 13 175 after eliminating 41 re-observed quasars.

(ii) With this combined sample, we have estimated a value for the possible variation of the fine-structure constant of  $\Delta\alpha/\alpha = (0.9 \pm 1.8) \times 10^{-5}$ , which represents the most accurate result obtained with this methodology.

(iii) We have also studied how much our results change when analysing the fiducial sample according to different properties (width, amplitude, S/N and  $R^2$  coefficient of the [O III] lines), and when modifying some parameters of the analysis (polynomial order for the continuum subtraction, different methods to determine the line position, e.g. Gaussian/Voigt profiles). We conclude that our results are quite robust, and they are consistent with no variation of the fine-structure constant.

(iv) From over one million simulated realizations of quasar spectra, we conclude that the precision of our emission-line method is dominated by the error from the Gaussian fits. Hence, the error from the continuum subtraction and any possible systematics from our code are small.

(v) The standard deviation of the results as a function of redshift correlates with the sky. This result suggests that our main source of uncertainty is determined by the sky subtraction algorithm.

(vi) We have determined the ratio of the [O III] transition lines to be  $2.96 \pm 0.02_{\text{sys}}$ , which is in good agreement with previous experimental and theoretical values.

(vii) The same systematic effect previously noticed by Gutiérrez & López-Corredoira (2010) has been found on the [Ne III] lines measurement. Incorrect measurement for the separation of the [Ne III] has been excluded as a possible explanation, and a blending of the H  $\epsilon$  and the [Ne III] 3968 has been identified as the source of this effect.

(viii) The measurement of  $\Delta\alpha/\alpha$  using SDSS-III/BOSS spectra has reached the maximum precision unless better sky subtraction algorithms are developed. To obtain better constraints ( $< 10^{-6}$ ) using the emission-line method, high-resolution spectroscopy ( $R \approx 100\,000$ ) is mandatory.

(ix) We note that future large galaxies survey like eBOSS or DESI could provide quite stringent constraint for  $\Delta\alpha/\alpha$  at low redshift, following our analysis of galaxy spectra taken from the DEEP2 survey.

## ACKNOWLEDGEMENTS

FDA, JC and FP acknowledge support from the Spanish MICINN's Consolider-Ingenio 2010 Programme under grant MultiDark CSD2009-00064, MINECO Centro de Excelencia Severo Ochoa Programme under grant SEV-2012-0249 and MINECO grants AYA-2012-31101 and AYA2014-60641-C2-1-P. FDA also acknowledges financial support from 'la Caixa'-Severo Ochoa doctoral fellowship, UAM+CSIC Campus of International Excellence and Instituto de Astrofísica de Canarias for a summer stay where this work began. AM and DAGH acknowledge support provided by the Spanish Ministry of Economy and Competitiveness (MINECO) under grant AYA-2011-27754.

Funding for SDSS-III has been provided by the Alfred P. Sloan Foundation, the Participating Institutions, the National Science Foundation, and the U.S. Department of Energy Office of Science. The SDSS-III web site is <http://www.sdss3.org/>.

SDSS-III is managed by the Astrophysical Research Consortium for the Participating Institutions of the SDSS-III Collaboration including the University of Arizona, the Brazilian Participation Group, Brookhaven National Laboratory, University of Cambridge, Carnegie Mellon University, University of Florida, the French Participation Group, the German Participation Group, Harvard University, the Instituto de Astrofísica de Canarias, the Michigan State/Notre Dame/JINA Participation Group, Johns Hopkins University, Lawrence Berkeley National Laboratory, Max Planck Institute for Astrophysics, Max Planck Institute for Extraterrestrial Physics, New Mexico State University, New York University, Ohio State University, Pennsylvania State University, University of Portsmouth, Princeton University, the Spanish Participation Group, University of Tokyo, University of Utah, Vanderbilt University, University of Virginia, University of Washington and Yale University.

This article is also partially based on service observations made with the Nordic Optical Telescope operated on the island of La Palma by the Nordic Optical Telescope Scientific Association in the Spanish Observatorio del Roque de Los Muchachos of the Instituto de Astrofísica de Canarias.

## REFERENCES

- Abazajian K. N. et al., 2009, *ApJS*, 182, 543  
 Adelman-McCarthy J. K. et al., 2008, *ApJS*, 175, 297  
 Alam S. et al., 2015, *ApJS*, 219, 12  
 Bahcall J. N., Salpeter E. E., 1965, *ApJ*, 142, 1677  
 Bahcall J. N., Schmidt M., 1967, *Phys. Rev. Lett.*, 19, 1294  
 Bahcall J. N., Sargent W. L. W., Schmidt M., 1967, *ApJ*, 149, L11  
 Bahcall J. N., Steinhardt C. L., Schlegel D., 2004, *ApJ*, 600, 520  
 Bolton A. S. et al., 2012, *AJ*, 144, 144  
 Bowen I. S., 1955, *ApJ*, 121, 306  
 Chand H., Petitjean P., Srianand R., Aracil B., 2005, *A&A*, 430, 47  
 Clifton T., Ferreira P. G., Padilla A., Skordis C., 2012, *Phys. Rep.*, 513, 1  
 Dawson K. S. et al., 2013, *AJ*, 145, 10

- Delubac T. et al., 2015, *A&A*, 574, A59  
 Díaz-Luis J. J., García-Hernández D. A., Kameswara Rao N., Machado A., Cataldo F., 2015, *A&A*, 573, A97  
 Dirac P. A. M., 1937, *Nature*, 139, 323  
 Eisenstein D. J. et al., 2011, *AJ*, 142, 72  
 Evans T. M. et al., 2014, *MNRAS*, 445, 128  
 García-Berro E., Isern J., Kubyshev Y. A., 2007, *A&AR*, 14, 113  
 Grupe D., Pradhan A. K., Frank S., 2005, *AJ*, 130, 355  
 Gunn J. E. et al., 2006, *AJ*, 131, 2332  
 Gutiérrez C. M., López-Corredoira M., 2010, *ApJ*, 713, 46  
 King J. A., Webb J. K., Murphy M. T., Flambaum V. V., Carswell R. F., Bainbridge M. B., Wilczynska M. R., Koch F. E., 2012, *MNRAS*, 422, 3370  
 Kramida A. E., Nave G., 2006, *Eur. Phys. J. D*, 37, 1  
 Landau S. J., Scócola G., 2010, *A&A*, 517, A62  
 Leal P. M. M., Martins C. J. A. P., Ventura L. B., 2014, *Phys. Rev. D*, 90, 027305  
 Maeda K.-I., 1988, *Mod. Phys. Lett. A*, 3, 243  
 Molaro P. et al., 2013, *A&A*, 555, A68  
 Moorwood A. F. M., Salinari P., Furniss I., Jennings R. E., King K. J., 1980, *A&A*, 90, 304  
 Newman J. A. et al., 2013, *ApJS*, 208, 5  
 Olive K. A., Pospelov M., Qian Y.-Z., Coc A., Cassé M., Vangioni-Flam E., 2002, *Phys. Rev. D*, 66, 045022  
 Petrov Y. V., Nazarov A. I., Onegin M. S., Petrov V. Y., Sakhnovsky E. G., 2006, *Phys. Rev. C*, 74, 064610  
 Pettersson S.-G., 1982, *Phys. Scr.*, 26, 296  
 Planck Collaboration XVI, 2014, *A&A*, 571, A16  
 Rahmani H., Maheshwari N., Srianand R., 2014, *MNRAS*, 439, L70  
 Savedoff M. P., 1956, *Nature*, 178, 688  
 Schneider D. P. et al., 2010, *AJ*, 139, 2360  
 Smee S. A. et al., 2013, *AJ*, 146, 32  
 Storey P. J., Zeippen C. J., 2000, *MNRAS*, 312, 813  
 Stoughton C. et al., 2002, *AJ*, 123, 485  
 Thompson R. I., 2012, *MNRAS*, 422, 67  
 Uzan J.-P., 2003, *Rev. Mod. Phys.*, 75, 403  
 Uzan J.-P., 2011, *Living Rev. Relativ.*, 14, 2  
 Whitmore J. B., Murphy M. T., 2015, *MNRAS*, 447, 446  
 York D. G. et al., 2000, *AJ*, 120, 1579

## SUPPORTING INFORMATION

Additional Supporting Information may be found in the online version of this article:

(<http://mnras.oxfordjournals.org/lookup/suppl/doi:10.1093/mnras/stv1406/-/DC1>).

Please note: Oxford University Press are not responsible for the content or functionality of any supporting materials supplied by the authors. Any queries (other than missing material) should be directed to the corresponding author for the article.

## APPENDIX A

We publish along with this paper an electronic table with the combined SDSS-III/BOSS DR12 and SDSS-II/DR7 sample of 13 175 quasars used in this work. Table A1 describes the information and format of each column.

**Table A1.** Description of the electronic table with the combined sample (13 175 quasars) published along with the paper.

| Column | Name         | Format | Description  |
|--------|--------------|--------|--|
| 1      | SDSS_NAME    | STRING | SDSS-DR12 designation hhmss.ss+ddmss.s (J2000)                           |
| 2      | RA           | DOUBLE | Right Ascension in decimal degrees (J2000)                               |
| 3      | DEC          | DOUBLE | Declination in decimal degrees (J2000)                                   |
| 4      | THING_ID     | INT32  | Thing_ID   |
| 5      | PLATE        | INT32  | Spectroscopic plate number   |
| 6      | MJD          | INT32  | Spectroscopic MJD (>55000 SDSS-III/BOSS spectra, <55000 SDSS-II spectra) |
| 7      | FIBER        | INT32  | Spectroscopic fibre number   |
| 8      | Z_VI         | DOUBLE | Redshift from visual inspection  |
| 9      | Z_PIPE       | DOUBLE | Redshift from BOSS pipeline  |
| 10     | ERR_ZPIPE    | DOUBLE | Error on BOSS pipeline redshift  |
| 11     | ALPHA        | FLOAT  | $\Delta\alpha/\alpha$ from the Gaussian fits                             |
| 12     | ERR_ALPHA    | FLOAT  | Standard error for $\Delta\alpha/\alpha$ from the Gaussian fits          |
| 13     | SN_01        | FLOAT  | S/N for the [O III] 4960 line  |
| 14     | SN_02        | FLOAT  | S/N for the [O III] 5008 line  |
| 15     | O1_FIT       | FLOAT  | Line centroid for the [O III] 4960 line                                  |
| 16     | O2_FIT       | FLOAT  | Line centroid for the [O III] 5008 line                                  |
| 17     | ERR_01       | FLOAT  | Error on the line centroid for the [O III] 4960 line                     |
| 18     | ERR_02       | FLOAT  | Error on the line centroid for the [O III] 5008 line                     |
| 19     | O1_AMPLITUDE | FLOAT  | Gaussian amplitude at the centre for the [O III] 4960 line               |
| 20     | O2_AMPLITUDE | FLOAT  | Gaussian amplitude at the centre for the [O III] 5008 line               |
| 21     | O1_WIDTH     | FLOAT  | Gaussian width for the [O III] 4960 line                                 |
| 22     | O2_WIDTH     | FLOAT  | Gaussian width for the [O III] 5008 line                                 |
| 23     | FILE_NAME    | STRING | File name to download from the SDSS server                               |

This paper has been typeset from a  $\text{\LaTeX}$  file prepared by the author.